

(12) INTERNATIONAL APPLICATION PUBLISHED UNDER THE PATENT COOPERATION TREATY (PCT)

(19) World Intellectual Property
Organization
International Bureau



(43) International Publication Date
1 December 2005 (01.12.2005)

PCT

(10) International Publication Number
WO 2005/114282 A2

(51) International Patent Classification⁷: **G02B 6/12**

(21) International Application Number:
PCT/US2005/017029

(22) International Filing Date: 13 May 2005 (13.05.2005)

(25) Filing Language: English

(26) Publication Language: English

(30) Priority Data:
60/571,416 13 May 2004 (13.05.2004) US
60/643,612 12 January 2005 (12.01.2005) US

(71) Applicant (for all designated States except US): **THE REGENTS OF THE UNIVERSITY OF CALIFORNIA** [US/US]; 1111 Franklin Street, 12th Floor, Oakland, CA 94607 (US).

(72) Inventors; and

(75) Inventors/Applicants (for US only): **YANG, Peldong** [CN/US]; 8118 Terrace Drive, El Cerrito, CA 94520 (US).

LAW, Mat [US/US]; 2807 Piedmont Avenue, Berkeley, CA 94705 (US). **SIRBULY, Donald, J.** [US/US]; 103 Crosby Court #4, Walnut Creek, CA 94598 (US). **JOHNSON, Justin, C.** [US/US]; 820 Kains Avenue #105, Albany, CA 94706 (US). **SAYKALLY, Richard** [US/US]; 14 Abbott Way, Piedmont, CA 94618 (US).

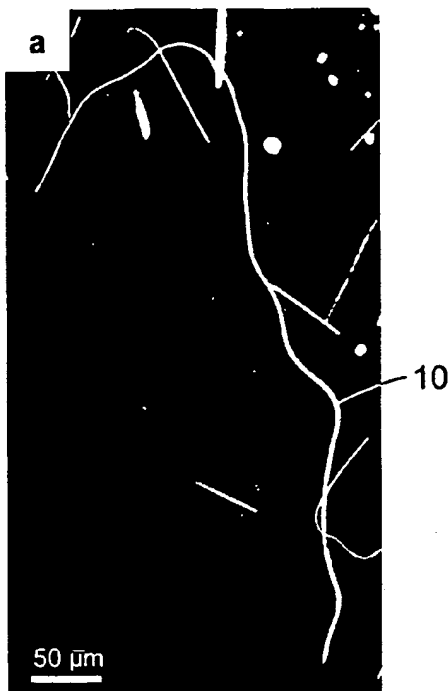
(74) Agent: **O'BANION, John, P.**; O'Banion & Ritchey LLP, Suite 1550, 400 Capitol Mall, Sacramento, CA 95814 (US).

(81) Designated States (unless otherwise indicated, for every kind of national protection available): AE, AG, AL, AM, AT, AU, AZ, BA, BB, BG, BR, BW, BY, BZ, CA, CH, CN, CO, CR, CU, CZ, DE, DK, DM, DZ, EC, EE, EG, ES, FI, GB, GD, GE, GH, GM, HR, HU, ID, IL, IN, IS, JP, KE, KG, KM, KP, KR, KZ, LC, LK, LR, LS, LT, LU, LV, MA, MD, MG, MK, MN, MW, MX, MZ, NA, NG, NI, NO, NZ, OM, PG, PH, PL, PT, RO, RU, SC, SD, SE, SG, SK, SL, SM, SY, TJ, TM, TN, TR, TT, TZ, UA, UG, US, UZ, VC, VN, YU, ZA, ZM, ZW.

(84) Designated States (unless otherwise indicated, for every kind of regional protection available): ARIPO (BW, GH,

[Continued on next page]

(54) Title: **NANOWIRES AND NANORIBBONS AS SUBWAVELENGTH OPTICAL WAVEGUIDES AND THEIR USE AS COMPONENTS IN PHOTONIC CIRCUITS AND DEVICES**



(57) Abstract: Nanoribbons and nanowires having diameters less than the wavelength of light are used in the formation and operation of optical circuits and devices. Such nanostructures function as subwavelength optical waveguides which form a fundamental building block for optical integration. The extraordinary length, flexibility and strength of these structures enable their manipulation on surfaces, including the precise positioning and optical linking of nanoribbon/wire waveguides and other nanoribbon/wire elements to form optical networks and devices. In addition, such structures provide for waveguiding in liquids, enabling them to further be used in other applications such as optical probes and sensors.

WO 2005/114282 A2



GM, KE, LS, MW, MZ, NA, SD, SL, SZ, TZ, UG, ZM, ZW), Eurasian (AM, AZ, BY, KG, KZ, MD, RU, TJ, TM), European (AT, BE, BG, CH, CY, CZ, DE, DK, EE, ES, FI, FR, GB, GR, HU, IE, IS, IT, LT, LU, MC, NL, PL, PT, RO, SE, SI, SK, TR), OAPI (BF, BJ, CF, CG, CI, CM, GA, GN, GQ, GW, ML, MR, NE, SN, TD, TG).

Published:

— without international search report and to be republished upon receipt of that report

For two-letter codes and other abbreviations, refer to the "Guidance Notes on Codes and Abbreviations" appearing at the beginning of each regular issue of the PCT Gazette.

**NANOWIRES AND NANORIBBONS AS SUBWAVELENGTH OPTICAL
WAVEGUIDES AND THEIR USE AS COMPONENTS
IN PHOTONIC CIRCUITS AND DEVICES**

5 **CROSS-REFERENCE TO RELATED APPLICATIONS**

[0001] This application claims priority from U.S. provisional application serial number 60/571,416 filed on May 13, 2004, incorporated herein by reference in its entirety, and from U.S. provisional application serial number 60/643,612 filed on January 12, 2005, incorporated herein by reference in its entirety.

10

**STATEMENT REGARDING FEDERALLY SPONSORED RESEARCH
OR DEVELOPMENT**

[0002] This invention was made with Government support under Contract No. DE-FG02-02ER-46021 awarded by the Department of Energy and Contract
15 No. DMR-0092086 awarded by the National Science Foundation. The Government has certain rights in this invention.

**INCORPORATION-BY-REFERENCE OF MATERIAL
SUBMITTED ON A COMPACT DISC**

20 **[0003]** Not Applicable

NOTICE OF MATERIAL SUBJECT TO COPYRIGHT PROTECTION

[0004] A portion of the material in this patent document is subject to copyright protection under the copyright laws of the United States and of other
25 countries. The owner of the copyright rights has no objection to the facsimile reproduction by anyone of the patent document or the patent disclosure, as it appears in the United States Patent and Trademark Office publicly available file or records, but otherwise reserves all copyright rights whatsoever. The copyright owner does not hereby waive any of its rights to have this patent
30 document maintained in secrecy, including without limitation its rights pursuant to 37 C.F.R. § 1.14.

BACKGROUND OF THE INVENTION

1. Field of the Invention

[0005] This invention pertains generally to optical waveguides, and more particularly to nanoribbons and nanowires employed as subwavelength optical waveguides as well as optical probes, sensors, routers and other devices based on nanoribbon/wire optical waveguides.

2. Description of Related Art

[0006] Chemically synthesized nanowires represent a unique class of building blocks for the construction of nanoscale electronic and optoelectronic devices. Since nanowire synthesis and device assembly are typically separate processes, nanowires permit more flexibility in the heterogeneous integration of different materials than standard silicon technology allows, although the assembly itself remains a major challenge. The toolbox of nanowire device elements is growing and currently includes various types of transistors, light emitting diodes, lasers, and photodetectors. While the electrical integration of simple nanowire circuits using lithography has been demonstrated, optical integration, which promises higher speeds and greater device versatility, remains unexplored.

[0007] Photonics, the optical analogue of electronics, shares the logic of miniaturization that drives research in semiconductor and communications technology. The ability to manipulate pulses of light within sub-micron spaces is vital for highly integrated light-based devices, such as optical computers, to be realized. Recent advances in using photonic bandgap and plasmonic phenomena to control the flow of light are impressive in this regard. However, both of these approaches typically rely on difficult and costly lithographic processes for device fabrication and are in early stages of understanding and development.

BRIEF SUMMARY OF THE INVENTION

[0008] A potentially simpler and equally versatile concept is to assemble photonic circuits from a collection of nanoribbon/nanowire elements that assume different functions, such as light creation, routing and detection. Accordingly, the present invention generally comprises a subwavelength

optical waveguide formed from a nanoribbon or nanowire having a diameter that is less than the wavelength of light to be guided. Such a subwavelength waveguide can serve a fundamental element of photonic circuits of various types.

5 **[0009]** Chemically synthesized nanoribbons and nanowires have several features that make them good building blocks, including inherent one-dimensionality, a variety of optical and electrical properties, good size control, low surface roughness and, in principle, the ability to operate both above and below the diffraction limit. An important step toward integrated
10 nanoribbon/wire photonics is to develop a nanoribbon/wire waveguide that can couple pairs of nanoribbon/wire elements and provide the flexibility in interconnection patterns that is needed to carry out complex tasks, such as logic operations.

15 **[0010]** Accordingly, one aspect of the invention is the assembly of photonic circuit elements from nanostructures such as SnO₂ nanoribbon and ZnO nanowire waveguides. In one embodiment, high aspect ratio (e.g., >1000) nanoribbons/nanowires with diameters below the wavelength of light (typically 100 nm to 400 nm) are used as waveguides of both their own internally generated photoluminescence (PL) and nonresonant UV/visible light emitted
20 from adjacent, evanescently coupled, nanoribbons/wires or external laser diodes

25 **[0011]** According to another aspect of the invention, the length, flexibility and strength of these single-crystalline structures enable them to be manipulated and positioned on surfaces to create various single-ribbon shapes and multi-ribbon optical networks, including ring-shaped directional couplers and nanoribbon/wire emitter-waveguide-detector junctions.

30 **[0012]** Another aspect of the invention is that the ability to manipulate the shape of active and passive nanoribbon/wire cavities provides a new tool for investigating the cavity dynamics of subwavelength structures. Moreover, future advances in assembling the diverse set of existing nanowire building blocks could lead to a novel and versatile photonic circuitry.

[0013] Another aspect of the invention is that nanoribbons/nanowires push

subwavelength optical fibers beyond silica. The scores of materials that can be made in nanoribbon/wire form include active, passive, nonlinear and semiconducting inorganic crystals, as well as a wide variety of polymers. Simultaneous photon, charge carrier and spin manipulation is possible within and between nanowires of different compositions. Also, many of these materials have higher refractive indices than silica-based glasses, permitting light of a given wavelength to be confined within thinner structures for denser integration.

[0014] Another aspect of the invention is waveguiding in liquids using subwavelength nanoribbon/wire optical waveguides.

[0015] According to another aspect of the invention, nanoribbons/wires are freestanding, mechanically flexible elements that can be manipulated on surfaces or used as mobile probes in fluids. As such, they offer a type of versatility difficult to achieve with lithographically-defined structures that are permanently affixed to their substrates.

[0016] Another aspect of the invention is a nanoribbon/wire optical waveguide having a high aspect ratio and a diameter less than the wavelength of light to be guided. In one embodiment, the aspect ratio is greater than approximately 1000. In another embodiment, the diameter is in the range of approximately 100 nm to approximately 400 nm.

[0017] Another aspect of the invention is a subwavelength optical waveguide formed from a crystalline oxide nanoribbon/wire. In one embodiment, the nanoribbon/wire comprises SnO_2 . In another embodiment, the nanoribbon/wire comprises ZnO . In still another embodiment, the nanoribbon/wire comprises GaN .

[0018] Another aspect of the invention is to provide a nanoribbon/wire laser and a nanoribbon/wire photodetector coupled by a nanoribbon/wire optical channel.

[0019] Another aspect of the invention is an optical waveguide comprising a nanoribbon/wire dispersed on an SiO_2 or mica substrate.

[0020] Another aspect of the invention is a method of forming a SnO_2 nanoribbon/wire waveguide.

[0021] Another aspect of the invention is a method of forming a ZnO nanoribbon/wire waveguide.

[0022] A further aspect of the invention is an apparatus for guiding light through liquid media, comprising a nanoribbon or nanowire waveguide. In one embodiment, the nanoribbon waveguide comprises a SnO₂ nanoribbon waveguide. In another embodiment, the nanowire waveguide comprises a ZnO nanowire waveguide. In a further embodiment, the waveguides comprise high dielectric waveguides. In still another embodiment, the nanowire waveguide comprises a GaN nanowire waveguide.

[0023] Another aspect of the invention is a probe or a sensor comprising a subwavelength nanostructure waveguide.

[0024] A further aspect of the invention is an optical router comprising at least two coupled nanoribbon waveguides. In one embodiment, the nanoribbon waveguides comprise SnO₂ nanoribbon waveguides.

[0025] Another aspect of the invention is an optical router comprising at least two coupled nanowire waveguides. In one embodiment, the nanowire waveguides comprise ZnO nanowire waveguides.

[0026] Still another aspect of the invention is an optical router comprising a network of nanoribbon waveguides configured to separate white light and route individual colors based on a short-pass filtering effect. In one embodiment, the nanoribbon waveguides comprise SnO₂ nanoribbon waveguides.

[0027] Another aspect of the invention is an optical crossbar grid comprising two pairs of orthogonal nanoribbon waveguides configured to conduct light through abrupt 90° angles. In one embodiment, the nanoribbon waveguides comprise SnO₂ nanoribbon waveguides.

[0028] Further aspects of the invention will be brought out in the following portions of the specification, wherein the detailed description is for the purpose of fully disclosing preferred embodiments of the invention without placing limitations thereon.

BRIEF DESCRIPTION OF THE SEVERAL VIEWS
OF THE DRAWING(S)

- [0029] The invention will be more fully understood by reference to the following drawings which are for illustrative purposes only:
- 5 [0030] FIG. 1A-C illustrate optical waveguiding in a 715 μm long SnO_2 nanoribbon.
- [0031] FIG. 2A-F illustrate panchromatic waveguiding in a 425 μm long nanoribbon.
- [0032] FIG. 3A-G illustrate shape manipulation of nanoribbon waveguides.
- 10 [0033] FIG. 4A-H illustrate an ~ 600 μm long nanoribbon slightly suspended above a substrate that undergoes physical manipulation by an etched tungsten probe.
- [0034] FIG. 5A-F illustrate dark-field images taken before and after manipulating a nanoribbon's cavity shape.
- 15 [0035] FIG. 6A-C illustrate nanoribbon coupling, optical components and devices.
- [0036] FIG. 7A-C show optical coupling between a ZnO nanowire and a SnO_2 nanoribbon waveguide.
- [0037] FIG. 8A-B show a hetero-junction created between a single ZnO
20 nanowire and a SnO_2 nanoribbon.
- [0038] FIG. 9A-C show a $\text{SnO}_2/\text{SnO}_2$ junction created by coupling two nanoribbon waveguides at their end facets.
- [0039] FIG. 10A-B illustrates nanoribbon short-pass filters.
- [0040] FIG. 11A-C illustrate waveguiding in water.
- 25 [0041] FIG. 12A-B show dark field images of waveguiding in water.
- [0042] FIG. 13A-D shows fluorescence and absorbance detection of R6G with a nanoribbon cavity.
- [0043] FIG. 14A-C illustrate the concept of SERS sensing with subwavelength waveguides.
- 30 [0044] FIG. 15 shows PL/dark-field image of two nanoribbons (NR1 and NR2) evanescently coupled at arrow 1.
- [0045] FIG. 16A-C illustrate the integration of waveguides into a fluidic device.

- [0046] FIG. 17A-F illustrate the routing of GaN PL and lasing emission.
- [0047] FIG. 18A-B illustrate multi-laser waveguiding.
- [0048] FIG. 19A-B illustrate GaN nanowire lasing.
- [0049] FIG. 20A-E show color filtering in a nanoribbon network.
- 5 [0050] FIG. 21 is a typical PL spectrum of a SnO₂ nanoribbon, showing its two defect bands.
- [0051] FIG. 22A-B illustrate optical routing in a rectangular nanoribbon grid.

DETAILED DESCRIPTION OF THE INVENTION

- [0052] Nanoscale ribbon-shaped crystals of binary oxides exhibit a range of
10 interesting properties including extreme mechanical flexibility, surface-mediated electrical conductivity, and lasing. However, as part of a recent study of the photoluminescence (PL) of SnO₂ nanoribbons in our laboratory, we discovered that nanoribbons with high aspect ratios (>1000) act as excellent waveguides of their visible PL emission. SnO₂ is a wide-bandgap
15 (3.6 eV) semiconductor characterized by PL bands at 2.5 eV (green) and 2.1 eV (orange), and finds application in gas sensors and transparent electrodes. For our studies, we used conventional thermal transport techniques to synthesize single-crystalline nanoribbons of SnO₂ with lengths of up to 5000 μm . The structures synthesized possessed fairly uniform (+/- 10%)
20 rectangular cross-sections with dimensions as large as 2 μm x 1 μm and as small as 15 nm x 5 nm. Many of the nanoribbons we synthesized were 100 nm to 400 nm wide and thick, which we found to be an optimal size range for efficient steering of visible and ultraviolet light in a subwavelength cavity.
- [0053] Additionally, we have found that photonic circuit elements can be
25 assembled from, for example, SnO₂ nanoribbon and ZnO nanowire waveguides. High aspect ratio nanoribbons/wires with diameters below the wavelength of light (typically 100 nm to 400 nm) were found not only to act as excellent waveguides of both their own internally generated photoluminescence (PL), but also nonresonant UV/visible light emitted from
30 adjacent, evanescently coupled, nanowires or external laser diodes. Furthermore, the length, flexibility and strength of these single-crystalline structures enable them to be manipulated and positioned on surfaces to

create various single-ribbon shapes and multi-ribbon optical networks, including ring-shaped directional couplers and nanowire emitter-waveguide-detector junctions. This ability to manipulate the shape of active and passive nanowire cavities provides a new tool for investigating the cavity dynamics of subwavelength structures. Moreover, future advances in assembling the diverse set of existing nanowire building blocks could lead to a novel and versatile photonic circuitry.

[0054] Note that the use nanoribbons/wires as optical waveguides is based on the nanoribbons/wires having diameters which are smaller than the wavelength of light. Note also that nanoribbons/wires may not have circular cross-sections. For example, ZnO nanowires typically have a hexagonal cross-section and SnO₂ nanoribbons typically have a rectangular cross-section. Therefore, in the case of a non-circular cross-section, the term "diameter" is intended generally to refer to the effective diameter, as defined by the average of the major and minor axis of the cross-section of the structure. However, the term "diameter" is not limited to the foregoing definition and is also intended to encompass dimensions of a nanoribbon/wire which allow for the nanoribbon/wire to function as a subwavelength waveguide.

20 [0055] Nanoribbon Waveguides

[0056] Initially, we studied the waveguiding behavior of individual nanoribbons dispersed on SiO₂ and mica substrates using far-field microscopy and spectroscopy. FIG. 1 and FIG. 2 illustrate representative data collected from single nanoribbons with lengths of 715 and 425 μm , respectively.

25 [0057] More particularly, FIG. 1 illustrates optical waveguiding in a 715 μm long SnO₂ nanoribbon that we synthesized. FIG. 1A is a dark-field image of a (350 nm wide by 245 nm thick) meandering nanoribbon 10 and its surroundings. The scale bar shown is 50 μm . FIG. 1B is the PL image of the nanoribbon under laser excitation. Here, the laser was focused to a spot size of $\sim 50 \mu\text{m}$ at a 30° incidence angle at the top end of the nanoribbon. FIG. 1C shows the spectra of the emission from the bottom terminus of the waveguide, collected at room temperature and at 5 K. A higher resolution emission profile

30

(inset) shows fine structure in three of the central peaks. This fine structure was found to be present in every peak.

[0058] FIG. 2 illustrates panchromatic waveguiding in a 425 μm long nanoribbon. FIG. 2A is a dark-field image of the nanoribbon 12, which has cross-sectional dimensions of 520 nm x 275 nm. The scale bar is 50 μm . FIG. 2B is a PL image with the UV excitation spot centered near the middle of the nanoribbon, showing waveguided emission from both ends. FIG. 2C is a magnified dark-field PL view of the right end of the nanoribbon, with the laser focused on the left end. A wide ($\sim 1 \mu\text{m}$) nanoribbon 14 lies across the nanoribbon of interest. The inset in FIG. 2C is a scanning electron micrograph of the right terminus of the nanoribbon, showing its rectangular cross-section. The scale bar is 500 nm. FIG. 2D, FIG. 2E and FIG. 2F are digital images of the guided emission 16a, 16b, 16c, respectively, at the output end of the nanoribbon during nonresonant excitation of the input end of the nanoribbon with monochromatic light of wavelengths 652 nm (red), 532 nm (green) and 442 nm (blue) light, respectively. The leftmost emission spots 18a, 18b, 18c in FIG. 2D, FIG. 2E and FIG. 2F, respectively, were caused by scattering at the nanoribbon-nanoribbon junction and were quenched by selectively removing the wide nanoribbon 14 with a micromanipulator.

[0059] As can be seen, when we tightly focused continuous wave laser light (3.8 eV) onto one end of a nanoribbon, a large fraction of the resulting PL was guided by the nanoribbon cavity to its opposite end, where the PL emanated with high intensity. Quite surprisingly, we found that the nanoribbon mimicked a conventional optical fiber. We also found that nanoribbons that were damaged internally during dispersion or which possessed sizeable 3D surface defects scattered guided light in a series of bright spots along their lengths. Referring to FIG. 2C, contact points between nanoribbons were often dark, although overlying nanoribbons, if thick, sometimes acted as scattering centers.

[0060] Referring again to FIG. 1C, we also found that emission spectrum collected from the end of a nanoribbon while exciting its opposite end often featured complex, quasi-periodic modulation. This is due to the transverse

modes allowed in a planar waveguide resulting from interference of electromagnetic waves resonating within the rectangular cavity (i.e., an optical mode structure). We found this modulation typically to be confined to the green PL component in cases of simultaneous green and orange emission, which suggests a difference in either the spatial location of PL emission (i.e., bulk vs. surface) or confinement of the two colors in the nanoribbon cavities. In short nanowire waveguides, such modulation is due to longitudinal Fabry-Perot type modes, with a mode spacing $\Delta\lambda$ given by $\Delta\lambda = \lambda^2 / \{2L[n - \lambda(dn/d\lambda)]\}$, where λ is the wavelength, L is the cavity length, and n is the index of refraction (2.1 for SnO_2). The nanoribbons, however, were so long that $\Delta\lambda$ was below the 0.01 nm resolution limit of our instrumentation. In addition, SnO_2 cavities are unlikely to show longitudinal modes since the reflectivity of their end facets is low ($\leq 13\%$) and there is no gain to compensate for scattering and output-coupling losses. A systematic study of the spectral structure is complicated by the complex dependence of the modes on nanoribbon cross-sectional size and orientation (through bend losses, substrate coupling and variations in refractive index), as well as on light intensity and end facet roughness. We note that the existence of a mode structure indicates that nanoribbon cavities can have high finesse. In addition, as discussed below, the loss at given wavelengths can be modified by distorting the cavity shape.

[0061] In general, one would expect a subwavelength resonator to show a large optical loss that is highly wavelength dependent, with better confinement of shorter wavelength radiation. To investigate the dependence of optical confinement on wavelength, we illuminated single nanoribbons with monochromatic red, green and blue light at a 30° incidence angle and monitored their end emission. We found that red waveguiding was rare, green waveguiding was common, and blue waveguiding was ubiquitous. We also found that, for a given dielectric material, cavity geometry and wavelength, there exists a critical diameter below which all higher order optical modes are cut off and waveguiding becomes increasingly difficult to sustain. More specifically, by treating a nanoribbon waveguide as a cylinder of SnO_2

embedded in air, we found cutoff diameters for higher order transverse modes of about 270 nm, 220 nm and 180 nm for the 652 nm, 532 nm and 442 nm light used in our experiment, respectively. While this approximation simplifies the cavity shape and ignores substrate coupling and other effects, these values are in reasonable agreement with scanning electron microscopy measurements of the sizes of the blue and green waveguides. Most of the nanoribbons in our samples were too thin to propagate red light over distances greater than approximately 100 μm . However, we clearly found that nanoribbons with sufficiently large cross-sectional dimensions as described above would effectively guide wavelengths across the visible spectrum, acting as subwavelength red-green-blue (RGB) optical fibers (e.g., optical transmitters) as shown in FIG. 2D through FIG. 2F.

[0062] Wavelength-Dependent Loss

[0063] We quantified the wavelength-dependent loss of straight nanoribbons using near-field scanning optical microscopy (NSOM). To do so, nanoribbons were pumped (3.8 eV) at different points along their length relative to a fixed collection probe. We found that losses ranged from 1-8 dB mm^{-1} for wavelengths between 450 nm and 550 nm, depending on nanoribbon cross-sectional area and the density of surface scattering centers. These values are higher than those reported recently for subwavelength silica waveguides, likely due to the relatively rougher nanoribbon surfaces and the extra loss due to substrate coupling. We note, however, that the losses here are better than what is required for integrated planar photonic applications, in which waveguide elements would transmit light over very short distances.

[0064] Shape Manipulation

[0065] We also found the nanoribbons to be of sufficient length and strength to be pushed, bent and shaped using a commercial micromanipulator under an optical microscope. The large aspect ratio and elastic flexibility of SnO_2 nanoribbons allowed us to manipulate the location and shape of individual nanoribbons under the optical microscope using a commercial micromanipulator tipped with sharp tungsten probes. Waveguiding nanoribbons with one end dangling in air could be elastically bent to large

angles (e.g., up to about 180°) without kinking or fracturing, which is remarkable for an oxide that is brittle in its bulk form. We were able to fashion straight nanoribbons into wiggles, circles and other shapes by using nanoribbon-substrate forces to prevent elastic recoil.

5 **[0066]** The dragging, aligning and cutting of single nanoribbons is routine. Here, we used the micromanipulator to selectively remove the overlying nanoribbon in FIG. 2C and quench scattering from that nanoribbon-nanoribbon interface. We later diced the long nanoribbon into three equal segments, creating three excellent waveguides.

10 **[0067]** FIG. 3 through FIG. 5 illustrate experimental results of our shape manipulation of nanoribbon waveguides. If these crystalline nanoribbon waveguides are to be useful as interconnects in optical circuits, they need to be capable of coupling light from one nano-object to another and to be facilely transportable from one location to another. To realize the latter, we attempted
15 to bend and move the nanoribbons using the micromanipulator.

[0068] FIG. 3A is an SEM image of a simple shape 20, demonstrating the high level of positional control afforded by the micromanipulator. This shape was created from a single straight nanoribbon of dimensions 400 nm x 115 nm that was cut into two pieces and then assembled. FIG. 3B and FIG. 3C are optical
20 images of the emission end of a long nanoribbon (aspect ratio ~ 5200), showing the minimal effect of curvature on waveguiding. FIG. 3B is a black and white rendering of a true color photograph taken after crafting a single bend. FIG. 3C is a black-and-white dark-field/PL image captured after an S-turn was completed. We found that blue light could be guided around 1 μm
25 radii curves with low loss. The SEM image in the inset of FIG. 3C resolves the bent geometry. FIG. 3D through FIG. 3F are a series of dark-field images and FIG. 3G is the corresponding guided PL spectra for a single nanoribbon 22 bent into different shapes. Collection was at the right end of the nanoribbon in each case. An unguided PL spectrum of the nanoribbon is included for
30 reference. Spectra are normalized and offset for clarity.

[0069] It will be appreciated that freestanding nanoribbons can be repeatedly and elastically curved into loops with radii as small as 5 μm, which is

remarkable for a crystal that is brittle in its bulk form. On appropriately chosen surfaces, single nanoribbons are easily fashioned into a variety of shapes with the help of nanoribbon-substrate forces to prevent elastic recoil as shown in FIG. 3A. Careful manipulation is normally nondestructive to the nanoribbon
5 cavities. In practice, this manipulation method is applicable to nanostructures that are free to move and visible using dark-field microscopy, including, at the lower size limit, short nanowires (e.g., 40 nm x 3 μ m) and even large nanocrystals. Though an inherently slow serial process, it is faster and more versatile than similar approaches using, for instance, scanning probes or in
10 situ scanning electron microscopy manipulation. We can create networks of nanoribbon waveguides and build functioning optoelectronic devices by assembling individual nanowire elements one at a time.

[0070] Manipulation also makes it possible to investigate the shape-dependent waveguiding of single nanoribbon cavities. For example, we fashioned a tight
15 S-turn in one end of a long, thin nanoribbon (dimensions: 785 μ m x 275 nm x 150 nm) to illustrate the robust nature of optical steering in these structures as shown in FIG. 3B and FIG. 3C. Losses around the bends were small and did not noticeably reduce light output from the end of the nanoribbon. In general, we found that twists and bends with radii of curvature as small as 1 μ m do not
20 disrupt the ability of these subwavelength waveguides to channel light across hundreds of microns.

[0071] We also observed that bending a nanoribbon, even slightly, can dramatically change the mode structure of its output light as shown in FIG. 3D through FIG. 3G. This is most likely because a change in cavity curvature
25 and/or cavity-substrate coupling alters the interference pattern of propagating waves, resulting in the enhancement of some modes and the partial quenching of others. Our data also indicate that the emission pattern from a typical nanoribbon is spatially heterogeneous, as shown previously in ZnO nanowires. As a consequence, the far-field spectrum changes somewhat with
30 collection angle, though not enough to account for the complex modal variations seen in response to distortions of the cavity shape.

[0072] FIG. 4 shows an approximately 600 μ m long nanoribbon 24 slightly

suspended above the substrate, which undergoes physical manipulation by an etched tungsten probe. FIG. 4A, FIG. 4C, FIG. 4D and FIG. 4F are dark-field images during the bending process, from no bend (FIG. 4A) to a $> 90^\circ$ angle (FIG. 4F), illustrating the extreme flexibility of the nanoribbons. FIG. 4B, FIG. 4E and FIG. 4G are PL images taken at different bend angles. The excitation source was focused on the top terminus of the nanoribbon and light was guided through the bends to emerge at the bottom terminus. FIG. 4H illustrates spectra taken at the bottom terminus as a function of arbitrary bend angle. The curves identified as Bend 1, 2, and 3 in FIG. 4H correspond to the images in FIG. 4C, FIG. 4D and FIG. 4F, respectively. The mode structure was found to be significantly dependent on the size and shape of the cavity.

[0073] The dark field images (FIG. 4A, FIG. 4C, FIG. 4D and FIG. 4F) were taken during the process of bending a nanoribbon that was slightly suspended above the substrate. This was the first direct indication of the degree of flexibility of these oxide nanostructures. The corresponding PL images (FIG. 4B, FIG. 4E, and FIG. 4G) provide additional information on the waveguiding behavior of the cavity as the nanoribbon is bent to angles $> 90^\circ$. In addition to the optical images, spectra were taken from the waveguided terminus of the nanoribbon. FIG. 4H shows the resulting emission profiles as a function of arbitrary bend angle. It is apparent that the mode structure emerges as the semi-linear nanoribbon begins to take physical shape, and leads to the possibility of using these nanoribbons as high quality (Q) factor cavities. To further pursue and explore the limitations of physically perturbing these nanoribbons, we focused on thinner nanoribbons that still exhibited outstanding waveguiding properties.

[0074] FIG. 5 clearly demonstrates the potential of these structures in nanophotonic circuits. FIG. 5A and FIG. 5C are dark-field images taken before (FIG. 5A) and after (FIG. 5C) manipulating the cavity shape of a nanoribbon. The flexibility of the nanoribbon allows it to maintain its shape integrity even after the tungsten probe is removed. FIG. 5B and FIG. 5D are PL images of the shapes in FIG. 5A and FIG. 5C, respectively. Even with two sharp bends, the nanoribbon successfully guided the defect emission from the

left coupling end to the right terminus with minimal loss occurring at the bend apexes. FIG. 5E and FIG. 5F are dark-field/PL (FIG. 5E) and PL (FIG. 5F) images of a new nanoribbon that had its bottom terminus pinned up against itself by the manipulator's tip. The excitation spot is just visible at the top of the PL image and the bottom terminus is denoted by the bright spot just above the tungsten probe. Even under extreme curvatures of radius, these nanoribbons were found to maintain their physical structures and waveguiding properties.

[0075] The dark-field images (FIG. 5A and FIG. 5C) and corresponding PL images (FIG. 5B and FIG. 5D) show before and after illustrations of how these nanoribbons can be torqued into sharp wiggles and curves, while still maintaining the low loss properties of the originally shaped nanoribbon. FIG. 5E and FIG. 5F reveal that this physical manipulation can be taken even further. Here, the end terminus of a new nanoribbon is actually pinned up against itself with the manipulator probe, leaving an exceptionally small radius of curvature ($< 5 \mu\text{m}$) kink in the nanoribbon. Even with the tight bend and physical contact with itself, the nanoribbon did not exhibit any significant light loss due to scattering centers or cavity leakage. For conventional silica fibers, this poses a major problem. With a lower dielectric material, light confinement drastically breaks down as critical angles are surpassed. In addition, any physical contact with a material of like refractive index causes severe energy loss. Tin oxide, however, can achieve a higher internal confinement due to its higher index of refraction, nearly double that of silica (2.3 to 1.4), and its unequivocal property of minimizing loss at like-refractive index interfaces.

[0076] Nanoribbon Optical Couplers and Filters

[0077] Referring now to FIG. 6 through FIG. 9, nanoribbon waveguides can be coupled together to create optical networks that may form the basis of miniaturized photonic circuitry. The approximate size of a nanoribbon can be inferred from the color of its guided PL; namely, large nanoribbons are white, while small nanoribbons are blue. When a nanoribbon of average size is pumped nearer to one end, it shines blue at the far end and green at the near end, demonstrating the higher radiation losses for longer wavelengths.

Referring also to FIG. 10, this effect makes nanoribbons excellent short-pass filters with tunable cutoffs based on path length. We have identified nanoribbon filters spanning the 465 nm to 580 nm region that feature steep cutoff edges and virtually zero transmission of blocked wavelengths.

5 **[0078]** Since light diffracts in all directions when it emerges from a subwavelength aperture, nanoribbons must be in close proximity, and preferably in direct physical contact, to enable the efficient transfer of light between them. We tested various coupling geometries and found that a staggered side-by-side arrangement, in which two nanoribbons interact over a
10 distance of several micrometers, outperforms direct end-to-end coupling, which relies on scattering between end facets. Staggered nanoribbons separated by a thin air gap can communicate via tunneling of evanescent waves. It is also possible to bond two nanoribbons together by van der Waals forces, often simply by draping one over another, to create a robust optical
15 junction.

[0079] FIG. 6 is illustrative of nanoribbon coupling, optical components and devices. FIG. 6A is a black-and-white dark-field/PL image of two coupled nanoribbons 28, 30 (both nanoribbons are 750 nm x 250 nm, 630 μ m total length). Light is incident on the right terminus of the right nanoribbon 30 and
20 collected at the left terminus of the left nanoribbon 28. The arrow denotes the location of the junction. The SEM image in the inset of FIG. 6A resolves the junction layout. FIG. 6B illustrates raw emission spectra of the left nanoribbon 28 before (upper curve) and after (lower curve) forming the junction. The addition of the second nanoribbon and the junction lowered the output light
25 intensity by only 50%, while its modulation was retained. FIG. 6C is a black and white rendering of a true color PL image of a three-ribbon ring structure that functions as a directional coupler. The ring nanoribbon 32 (135 μ m x 540 nm x 175 nm) is flanked by two linear nanoribbons 34, 36 (34 at left, 120 μ m x 540 nm x 250 nm; 36 at right, 275 μ m x 420 nm x 235 nm). Light input at
30 branch 1 exits preferentially at branch 3 (as shown), while light input at branch 2 exits branch 4.

[0080] Note that FIG. 6A and FIG. 6B illustrate an example of two-ribbon

coupling. However, more functional geometries, such as Y-junctions, branch networks, Mach-Zehnder interferometers and ring oscillators can also be constructed. The three-ribbon ring structure illustrated in FIG. 6C operates by circulating light that is injected from one branch around a central cavity, which can be tapped by one or more output channels to act as an optical hub. With further integration, it should be possible to create optical modulators based on nanoribbon assemblies that utilize the electro-optic effect for phase shifting.

[0081] Single-crystalline nanoribbons are intriguing structures with which to manipulate light, both for fundamental studies and photonics applications. As passive elements, they are efficient UV/visible waveguides and filters that can be assembled into optical components, networks and devices. Being semiconductors or, in their doped state, transparent metals, oxide nanoribbons are well suited to combine simultaneous electron and photon transport in active nanoscale components. Key challenges to the wider use of these materials include narrowing their size dispersity and developing better parallel assembly schemes for nanowire integration. Answering the former challenge depends on gaining control over the poorly understood vapor-solid process that is typically used in nanoribbon synthesis.

[0082] FIG. 7 illustrates successful optical coupling between a ZnO nanowire 38 and a SnO₂ nanoribbon waveguide 40. FIG. 7A is a black and white rendering of a true color dark-field/PL image of the nanowire 38 (56 μm long, at top, pumped at 3.8 eV) channeling light into the nanoribbon 40 (265 μm long, at bottom). The arrow denotes the location of the junction. FIG. 7B is an SEM image of the nanowire/nanoribbon junction. FIG. 7C illustrates spectra of the coupled structures taken at different excitation and collection locations. From top to bottom: unguided PL of the ZnO nanowire; waveguided emission from the ZnO nanowire collected at the bottom terminus of the nanoribbon; waveguided emission from the SnO₂ nanoribbon excited just below the junction and collected at its bottom terminus; unguided PL of the SnO₂ nanoribbon. Note that the emission from the ZnO nanowire is modulated during its transit through the nanoribbon cavity.

[0083] FIG. 8 illustrates another example of a hetero-junction created between

a single ZnO nanowire and a SnO₂ nanoribbon. FIG. 8A is a dark-field image of the junction after pushing a ZnO nanowire up to the end facet of the SnO₂ nanoribbon. The inset in FIG. 8A is a magnification of the active coupling region showing the short (~ 6-7 μm) ZnO nanowire and the upper terminus of the SnO₂ nanoribbon. The total length of the nanoribbon was ~ 600 μm. FIG. 8B shows spectra collected at the passive end (bottom terminus) while pumping either the ZnO nanowire (On ZnO) or the SnO₂ nanoribbon directly (On NR). A profile of the band gap emission collected over the ZnO nanowire (ZnO Only) is included for reference. The Modulation in the "On ZnO" spectrum is a direct result of the broad emission from the ZnO propagating through a high Q-factor SnO₂ cavity.

[0084] The 50x dark-field image and 100x dark-field inset of FIG. 8A pictorially demonstrate the basic components of an active/passive nanophotonic device. However, to ensure that we had devised a complete junction between the two nanosystems, we optically pumped the ZnO nanowire active end and collected at the passive SnO₂ nanoribbon end. As seen in FIG. 8B, ZnO band gap emission created from the pump source was directed across the intervening air space by the ZnO cavity and into the neighboring SnO₂ waveguide. The light output from the ZnO nanowire emerged at the distant end of the nanoribbon and clearly showed a modulated emission profile similar to the PL line shape seen in FIG. 4. This provides good evidence that the light was in fact waveguided across hundreds of microns by the nanoribbon cavity. To build like-material junctions, we employed a similar manipulation scheme as described above. Two waveguiding nanoribbons were coupled with their long axes collinear to each other by physically sliding a larger nanoribbon directly adjacent to the far end of a smaller nanoribbon.

[0085] FIG. 9 illustrates a SnO₂/SnO₂ junction created by coupling two nanoribbon waveguides 42, 44 at their end facets. FIG. 9A and FIG. 9B are dark-field images before (FIG. 9A) and after (FIG. 9B) completing a junction between a large 42 (~ 1 μm) and small 44 (~ 400 nm) diameter nanoribbon. FIG. 9C is a PL image of the same nanoribbon junction and end terminus shown in FIG. 9B demonstrating that multi-junction networks between SnO₂

nanoribbon waveguides can be realized.

[0086] The dark-field images in FIG. 9A and FIG. 9B capture the junction before and after successfully adjoining the two nanoribbons. The PL image in FIG. 9C verifies that light traveling down the small nanoribbon can be directly coupled into a secondary like-cavity. We are now building all-nanowire optical circuits that operate via electron injection rather than optical pumping. The oxide waveguides serve as important interconnects between active light sources, such as LEDs and lasers, and optical detectors based on photoconducting nanowires.

10 [0087] The optical loss of several nanoribbon waveguides was measured by systematically varying the distance between UV excitation (50 μm spot size) and PL collection in the near-field. We estimate a loss of about 2 dB mm^{-1} at a wavelength of 550 nm for a nanoribbon with a 400 x 150 nm² cross-section, which is significantly greater than losses reported recently for subwavelength silica waveguides.

15 [0088] As can be seen from the forgoing, due to their extraordinary length, high flexibility and strength, nanoribbon waveguides are excellent materials with which to study the interplay between mechanics, microstructure and optical confinement in nanoscale cavities. They can be manipulated and assembled to serve as photonic interconnects between single nano-objects, such as nanowire lasers, in optical circuits and devices.

20 [0089] Furthermore, nanoribbon waveguides can be used as filter devices. For example, FIG. 10 illustrates the use of nanoribbons as short-pass filters. FIG. 10A shows room temperature PL spectra of five different nanoribbons, each 200 μm to 400 μm long, with 50% intensity cut-off wavelengths ranging from 465 nm to 580 nm. Cross-sectional dimensions of the 465 nm, 492 nm, 514 nm, 527 nm and 580 nm filters were 310 nm x 100 nm (0.031 μm^2), 280 nm x 120 nm (0.037 μm^2), 350 nm x 115 nm (0.04 μm^2), 250 nm x 225 nm (0.056 μm^2), and 375 nm x 140 nm (0.053 μm^2), respectively. The spectra were normalized and offset for clarity. FIG. 10B shows a series of normalized emission spectra taken of a single nanoribbon (315 μm x 355 nm x 110 nm)

25

30

as the pump spot was scanned away from the collection area. The unguided PL curve was obtained at a pump-probe separation of 50 μm . Larger separations resulted in a progressive loss of the long wavelengths.

[0090]

Example 1

5 [0091] SnO_2 nanoribbon waveguides were synthesized by the chemical vapor transport of SnO powder in a quartz tube reactor operating at 1100 °C and 350 Torr of flowing argon (50 sccm). Milligram quantities of nanoribbons were collected on an alumina boat near the center of the reactor and deposited onto clean substrates by dry transfer. Long ZnO nanowires were grown via
10 oxidation of Zn metal in a quartz furnace at 800 °C and 760 Torr of flowing oxygen/argon, as described in the literature, and also dispersed by dry transfer. InP nanowires produced by a laser-assisted vapor-liquid-solid process (using Au catalyst) were sonicated into ethanol solution and transferred to the surface by drop-casting. Contacts to InP were fabricated by
15 electron beam lithography and thermal evaporation (100 nm Ti), followed by rapid thermal annealing at 475 °C in N_2/H_2 for one minute.

[0092]

Example 2

[0093] Optical measurements were carried out using a dark-field microscope outfitted with a cryostat (Janis X-100). The PL excitation source was a HeCd
20 laser operating at 325 nm. Laser pointers (532 and 652 nm) and the HeCd laser (442 nm) provided nonresonant illumination. The size of the laser spot was $\sim 50 \mu\text{m}$ for all measurements. Spectra were collected with a fiber-coupled spectrometer (SpectraPro 300i, Roper Scientific) and liquid N_2 cooled CCD detector. Images were captured using both a microscope-mounted
25 camera (CoolSNAP, Roper Scientific) and a handheld digital camera (PRD-T20, Toshiba). Loss measurements were made with a commercial NSOM setup operating in collection mode, with 325 nm excitation. For nanoribbon manipulation, we used a three-axis commercial unit tipped with tungsten probes (10 μm ends).

30 [0094] As described above, photonic circuit elements can be assembled from SnO_2 nanoribbon and ZnO nanowire waveguides. High aspect ratio nanoribbons/wires with diameters below the wavelength of light (typically 100

nm to 400 nm) were shown to act as excellent waveguides of both their own internally generated photoluminescence (PL) and nonresonant UV/visible light emitted from adjacent, evanescently coupled, nanowires or external laser diodes. The length, flexibility and strength of these single-crystalline structures enabled them to be manipulated and positioned on surfaces to create various single-ribbon shapes and multi-ribbon optical networks, including ring-shaped directional couplers and nanowire emitter-waveguide-detector junctions. This ability to manipulate the shape of active and passive nanowire cavities provides a new tool for investigating the cavity dynamics of subwavelength structures. Moreover, future advances in assembling the diverse set of existing nanowire building blocks could lead to a novel and versatile photonic circuitry.

[0095] Waveguiding in Liquids

[0096] Quite surprisingly, we have also found that these one-dimensional (1D) nanostructures can guide light through liquid media. The fact that light can be delivered through these cavities in solution offers a unique application for high dielectric ($n \geq 2$) waveguides in fluidic sensing and probing. Waveguiding in liquids is especially important for integrated on-chip chemical analysis and biological spectroscopy in which small excitation and detection volumes are required. Subwavelength nanostructures can be assembled to probe molecules in a fluorescence or absorption scheme, both of which utilize the decaying light field outside of the cavity to induce photon absorption. The waveguide is strongly coupled to emitted photons near the cavity, allowing the generated fluorescence to be directed back to the point of injection. Also, the nanoscale dimensions of the waveguides afford small liquid volumes (~picoliters) to be sensed and presage the way for miniaturized optical spectrometers.

[0097] Here, we also build upon the initial demonstration of nanowire/ribbon photonic assembly with several proof-of-principle illustrations of optical routing between coupled nanowires. We first show that it is possible to deliver individual nanosecond light pulses from lasing GaN and ZnO nanowires

through a nanoribbon waveguide; pulsed light must be transmissible if nanowire photonic devices are to be useful in communications or computing. Simple networks of SnO₂ nanoribbons are then used to separate white light and route individual colors based on a short-pass filtering effect. We also describe an optical crossbar grid made of two pairs of orthogonal nanoribbons that conducts light through abrupt 90° angles and provides a dramatic example of the nature of optical confinement in these subwavelength cavities. The fact that the waveguiding ability of our freestanding, flexible nanowires and nanoribbons survives in liquid media suggests a role for nanowire light delivery in microfluidics and biological applications.

Subwavelength Waveguides as Optical Probes and Sensors

[0098] High dielectric subwavelength waveguides have a considerable advantage for confining light in liquids over low dielectric waveguides such as silica-based structures. The low index contrast between the solution (cladding) and silica core ($n_{\text{silica}} \approx 1.45$) hinders efficient propagation of the light wave. FIG. 11 compares the photoluminescence (PL)/dark-field images of a SnO₂ nanoribbon (dimensions: 365 nm x 105 nm x 265 μm) resting on a silicon oxide surface (1 μm thermal oxide) waveguiding in air ($n = 1$) and water ($n = 1.33$). The PL is generated with a CW HeCd laser (325 nm). FIG. 11 also shows how the guided PL spectrum of this thin nanoribbon changes when it is immersed in water.

[0099] FIG. 11A is a combined PL/dark-field image of the nanoribbon 46 on a dry oxide surface. The inset shows a magnified view of the blue end emission. FIG. 11B shows the same nanoribbon in a water environment, under a quartz coverslip. The inset shows resultant green emission. FIG. 11C shows the spectra of the two situations. The large red shift of the empirical cutoff wavelength (from 483 nm in air to ~570 nm in water) is caused by the decrease in refractive index profile between the substrate and the cap medium. The more homogeneous cladding index improves wave confinement in the nanoribbon core. The effect was reversible by evaporating the water.

[00100] As can be seen from FIG. 11C, the spectra of the guided PL spectrum broadens to longer wavelengths when it is covered by pure water. Such a red

shift would be anomalous for a fiber with a cladding of homogeneous refractive index, where one expects the replacement of air ($n=1$) by water ($n=1.33$) to increase losses and result in a blue shift of the mode cutoff. However, when a slab or strip waveguide exists in an asymmetric cladding environment (that is, when $n_{\text{waveguide}} > n_{\text{substrate}} > n_{\text{cover}}$), as it does here, raising the index of the cover reduces its asymmetry with the substrate and improves confinement.

[00101] Intuitively, the replacement of air ($n=1$) with water ($n=1.33$) on three sides of a nanoribbon should increase its optical loss and hinder waveguiding, especially for longer wavelengths. One would expect a narrowing of the guided spectrum (a blue shift of the cutoff wavelength). Instead, we found that the spectrum broadens to the red and the end emission changes from blue in air to green in water. This surprising result, which seems to suggest that a smaller index profile between core and cladding results in better, not poorer, confinement, is likely a consequence of the smaller difference in refractive index between water and the SiO_2 substrate than between air and the substrate. The less anisotropic water-silica cladding shifts the modal power nearer to the center of the nanoribbon and thereby reduces overall radiative loss. Ribbons that were too large to show a cutoff for PL were unaffected by immersion in water.

[00102] To demonstrate controlled manipulation of small volume, substrate supported, liquid droplets, we placed an approximately 5 μL droplet of 1,5-pentanediol on a silica substrate and then used a commercial micromanipulator, equipped with an etched tungsten probe (tip diameter ~ 400 nm), to dice the large droplet into small volumes as shown in FIG. 12. FIG. 12A shows a dark-field image of various sized droplets of 1,5-pentanediol on a silicon substrate (with a 1 μm thermal oxide). The radii and corresponding volumes are displayed by each droplet. FIG. 12B is a magnified dark-field image of smaller droplets (< 1 fL). The radii and corresponding volumes (down to ~ 20 fL) are labeled on the dark-field image in FIG. 12A. Even smaller volumes (< 1 fL) can be achieved with this method as shown in FIG. 12B. An alternative method to producing small volumes would be to use

microfluidic channels to mold the shape of the solution.

5 [00103] Ribbon waveguides can also sense molecules, proteins or larger biological entities in solution by means of either an emission or absorption mechanism as mentioned above. In the former, a nanoribbon provides local excitation for fluorophores passing through the cone of scattered light at its output end, and the emission is collected by a fiber or microscope.

10 [00104] Referring to FIG. 13, to demonstrate this fluorescence scheme, we embedded the tip of a nanoribbon 48 in an approximately 3 pL to 5 pL droplet of 1 mM Rhodamine 6G laser dye (R6G) in 1,5-pentanediol ($n = 1.45$). FIG. 13 shows fluorescence and absorbance detection of R6G with a nanoribbon cavity. FIG. 13A is a fluorescence image of a droplet of 1mM R6G in 1,5-pentanediol excited by blue light from a nanoribbon waveguide 48 (240 nm by 260 nm by 540 μm). The nanoribbon crosses the frame from upper left to lower right. A notch filter was used to block the excitation light. The left inset of FIG. 13A is a dark-field image showing the droplet and the bottom half of the nanoribbon. The right inset of FIG. 13A is a magnified view of the droplet emission, showing the light cone and evanescent pumping of the dye along the nanoribbon length. FIG 13B shows the spectra taken of the droplet region (direct) and the fluorescence coupled back into the nanoribbon (guided). The red shift of the guided emission is a microcavity effect. FIG. 13C is a dark-field image of the nanoribbon with a droplet deposited near its middle (absorbance geometry). The nanoribbon was UV pumped on one side of the droplet and probed on the other side, as indicated. FIG. 13D shows the spectra of the guided PL without liquid present and with droplets of pure 1,5-pentanediol and 1 mM R6G. The arrow indicates the absorption maximum of R6G.

20 [00105] As can be seen, blue light (442 nm) launched into the far end of the nanoribbon resulted in strong fluorescence from within the droplet, where the R6G emission mapped out the spatial intensity distribution of the waveguide output as a cone of light (FIG. 13A and Inset). A fraction of this fluorescence was captured by the nanoribbon cavity and guided back to its far end, demonstrating that these waveguides are capable of routing signals both from

30

and to liquids. Spectra acquired from both ends of the nanoribbon are shown in FIG. 13B. The guided fluorescence is red-shifted and somewhat sculpted by its passage through the nanoribbon. However, there is little trace of the heavy mode imprinting evident in, for example, FIG. 17F discussed below.

5 **[00106]** FIG. 13B also shows strong fluorescence originating from the segment of the nanoribbon wet by the droplet through capillary action. Here, dye molecules in proximity to the nanoribbon surface are excited in a subwavelength version of total internal reflection fluorescence (TIRF). In normal TIRF, excitation of a macroscopic waveguide (such as a microscope coverslip) generates an evanescent field of light that decays exponentially with
10 distance from the waveguide surface, limiting the depth of excitation to a distance of ~100 nm and enabling the local probing of structures such as cell membranes. Because subwavelength fibers can carry a larger fraction of their modal power outside of the core, they enhance the intensity of this
15 evanescent field and increase its penetration depth into the surroundings, making proportionally more power available to excite nearby molecules. Calculations indicate that roughly thirteen to fifteen per cent of the electric field intensity exists outside of the nanoribbon for the wavelength of light used in this experiment. In this case, the radial field intensity decays to ten per cent of
20 its maximum value at the center of the waveguide by about 135 nm into the liquid solution. Since TIRF detection sensitivity scales with the fractional power present in the waveguide cladding, one-dimensional nanostructures are promising waveguides for local fluorescence sensing using this approach.

[00107] Another way that 1D nanostructures may be used for optical detection
25 in solution relies on producing an absorption spectrum of molecules located on and near the nanoribbon surface. Absorbance detection, while inherently less sensitive than fluorescence methods, is applicable to a wider range of molecules and avoids the complications of fluorescent tagging. We launched white PL down a long nanoribbon (260 nm x 240 nm x 540 μ m) onto the
30 midpoint of which a ~1 μ L droplet of 1 mM R6G ($\alpha_{\text{max}} = 535$ nm) was deposited (FIG. 13C). Dye molecules in the droplet imprinted their absorption signature onto the propagating PL wave (double-Gaussian beam), completely

quenching transmission through the nanoribbon around the R6G absorption maximum (FIG. 13D). Considering the dye concentration, droplet size and spatial extent of the evanescent field, we estimate that less than forty attomoles of dye (~24 million molecules) were probed in this experiment. We have experimentally shown that sensitivities down to 50 μM (~35,000 molecules) are easily attainable. We were able to detect dye concentrations as low as 1 μM (24,000 molecules) using the same nanoribbon and a comparable path length of ~50 μm (not shown). Since this absorbance approach also utilizes the evanescent fraction of the guided field, smaller nanoribbons should again provide greater sensitivity. Other options for improvement include altering the cavity shape to increase the probe length (as discussed below), functionalizing the nanoribbon surface for selective biosensing and launching multiple wavelengths for the simultaneous detection of analytes with different electronic transitions. The next steps are to integrate subwavelength 1D nanostructures into microfluidic devices and to apply them as flexible probes in the study of live cells.

[00108] A third way that subwavelength nanoribbons/wires can be used for chemical/biological sensing relies on the surface enhanced Raman spectroscopic (SERS) effect. Surface-enhanced Raman scattering occurs when an analyte molecules is probed in proximity to a metal surface (usually Cu, Ag or Au) that serves to massively enhance the local electromagnetic field through resonance with the surface plasmons of the metal. The resulting Raman signal of the analyte can be enhanced by a factor of up to 10^{14} , which allows single-molecule sensing in many cases. The nanoribbons/wires described here were fashioned into subwavelength SERS fibers by decorating their surfaces with a high density of silver nanoparticles. By exposing the nanoparticles-coated nanoribbon/wire to an analyte solution while injecting monochromatic light down the nanoribbon/wire, it is possible to detect the SERS signal of the analyte molecule. This concept allows "fingerprint" identification of analyte molecules based on their SERS vibrational signatures, using a subwavelength waveguide for light introduction and confinement. FIG. 14A shows a schematic picture of this concept, while FIG. 14B and FIG. 14C

show an image of a nanoribbon (NR) coated with 40 nm silver nanoparticles attached by exposing the nanoribbon to a flowing nanoparticle solution. The particles are seen to scatter the waveguided light very effectively. By then exposing the structure to an analyte solution of interest, it is possible to generate a SERS signal. The device is reusable by simply dissolving the Ag nanoparticles in an acidic solution (e.g., HNO₃) and then reintroducing fresh Ag particles.

[00109] The devices shown thus far all operate under single pass geometries. Multi-pass structures would increase sampling lengths and ultimately lead to a more sensitive spectrometer. FIG. 15 shows a PL/dark-field image of two nanoribbons (NR1 and NR2) evanescently coupled at arrow 1. The top inset is a magnified dark-field image of the coupled nanoribbons with a glycol droplet designating where the analyte would sit in this configuration. The bottom inset is a dark-field image of NR1 with NR2 removed showing a coupled ring structure (junction – denoted be arrow 2) that would serve as a multi-pass beam path in a subwavelength optical spectrometer.

[00110] FIG. 15 illustrates that ring shapes can be easily fashioned using our manipulation capabilities to create a subwavelength cavity shape that would sample an analyte repetitively. The glycol droplet (top inset) serves to identify where the analyte would sit in this particular configuration. The PL/dark-field image shows a two nanoribbon device evanescently coupled (arrow 1 denotes the junction), illustrating the first step to design a multi-pass spectrometer based on free-standing 1D nanostructures. The bottom inset was taken after manipulating the end of NR1 into a ring structure (arrow 2 denotes the junction) showing the second step for creating a multi-cycle instrument. Additional work is necessary to fully realize better sensitivity from these advanced designs, but previous results on coupling efficiencies suggest up to an order of magnitude increase from a multi-pass geometry.

[00111] We note that the fabrication of a practical subwavelength fiber spectrometer as introduced above would benefit from a more controlled flow-cell type microfluidic design in which the sensing nanoribbon/wire is integrated with microfluidic channels for solution introduction. We have built such an

integrated device using a poly-dimethylsiloxane (PDMS) stamp patterned with flow channels to control analyte flow past an embedded nanoribbon/wire waveguide. With this microfluidic design, we can pulse multiple analyte solutions past a well-defined section of a sensing nanoribbon/wire, permitting reuse of the sensor for biological and other liquid-based monitoring uses. FIG. 16 shows the microfluidic channels (MFC) of a PDMS stamp bridged by multiple nanoribbons (NR). This is shown schematically in FIG. 16A. FIG. 16B is an image showing microfluidic channels in detail and FIG. 16C is an image showing several nanoribbons bridging the microfluidic channels shown in FIG. 16B. This microfluidic layout is important for the practical use of these structures for fluorescence, absorbance and SERS sensing.

[00112] It should be noted that the ideas and principles set forth herein for chemically synthesized 1D semiconductor nanostructures are entirely compatible with existing lithography techniques. State-of-the-art electron beam and other lithography methods currently offer better size control, reproducibility, and processing speeds to produce subwavelength optical probes and spectrometers than the serial approach discussed here. Future experiments will include lithographically defined structures on various support substrates to discern the limits of detection using nanoscale optics.

[00113] In terms of present industrial efforts and interests in small volume detection, NanoDrop[®] Technologies has developed a UV/Vis spectrometer (ND-1000) based on patented sample retention technology. The instrument is generally used to detect 1 μ L to 2 μ L nucleic acid aliquots with a sample detection limit of 2 ng/ μ L (dsDNA). The path length for the Xe flash lamp (220 nm to 750 nm) is held relatively fixed at 1 mm. The major advantages of a subwavelength spectrometer over the commercially available unit is smaller volume size ($\sim 10^6$ times smaller), shorter path lengths (~ 10 times shorter), and possibly higher sensitivity with the advanced multi-pass geometries.

Optical Routing With Nanoribbons And Nanowire Assemblies

[00114] The manipulation of optical energy in structures smaller than the wavelength of light is key to the development of integrated photonic devices for computing, communications and sensing. We assembled small groups of

freestanding, chemically synthesized nanoribbons and nanowires into model structures that illustrate how light is exchanged between subwavelength cavities made of three different semiconductors. The strength of the optical linkages formed when nanowires are brought into contact depends both on
5 their volume of interaction and angle of intersection. Using simple coupling schemes, lasing nanowires can launch coherent pulses of light through nanoribbon waveguides that are up to several millimeters in length. Also, inter-wire coupling losses are low enough to allow light to propagate across several right-angle bends in a grid of crossed nanoribbons. The fraction of the
10 guided wave power traveling outside the nanowire/nanoribbon cavities is utilized to link nanowires through space and to separate colors within multi-ribbon networks. In addition, we find that nanoribbons function excellently as waveguides in liquid media and provide a unique way to probe molecules in solution or in proximity to the waveguide surface. Our results lay the
15 groundwork for photonic devices based on assemblies of active and passive nanowire elements and presage the use of nanowire waveguides in microfluidics and biology.

[00115]

Example 3

[00116] SnO₂ nanoribbons were synthesized by the chemical vapor transport of
20 SnO at 1100°C in flowing argon. ZnO nanowires were grown as epitaxial arrays on sapphire substrates by the oxidation of metallic zinc at 800°C, using gold as a catalyst. GaN nanowires were made by the chemical vapor transport of gallium in a NH₃/H₂ mixture at 900°C, with nickel as the catalyst. The SnO₂ nanoribbons were dry transferred en masse to oxidized silicon
25 substrates (600 nm SiO₂, Silicon Sense Inc.). A triple-axis micromanipulator tipped with a tungsten probe (~400 nm tip diameter) was used to remove individual ZnO and GaN nanowires (chosen by their PL spectra) from their growth substrates and then deposit them with the nanoribbons.

[00117]

Example 4

30 [00118] Nanoribbons and nanowires were manipulated with the probe under a dark-field microscope. A HeCd laser provided continuous wave (CW) resonant illumination (325 nm), while the fourth-harmonic of a Nd:YAG laser (266 nm, 8

nm, 10 Hz) was used for pulsed pumping. Laser diodes (652 nm and 532 nm) and the HeCd laser (442 nm) supplied visible light for the filtering and fluorescence demonstrations. The lasers were focused to a beam diameter of approximately 50 μm , giving a CW power density of approximately 175 W/cm^2 and a pulsed energy density of approximately 10 $\mu\text{J}/\text{cm}^2$. Spectra were acquired with a fiber-coupled spectrometer (gratings at 150 and 1200 grooves/mm, SpectraPro 300i, Roper Scientific) and liquid N_2 -cooled CCD setup. Black-and-white and color images were recorded with two microscope-mounted CCD cameras (CoolSnap fx and CoolSnap cf, Photometrics).

10 **[00119]** Many of the nanoribbons/wires described herein operated as single-mode fibers for some of the experimental wavelengths, while others were multi-mode. For reference, the approximate single-mode cutoff diameters of a cylindrical step-index fiber in air are 140 nm ($\lambda = 365$ nm) and 265 nm ($\lambda = 600$ nm) for SnO_2 , 112 nm ($\lambda = 365$ nm) for GaN, and 140 nm ($\lambda = 380$ nm) and 220 nm ($\lambda = 510$ nm) for ZnO .

[00120] In the liquid experiments, large droplets (~ 5 μL) of water or various alcohols were transferred to the oxide surface by pipette. The solvent droplets were then diced into smaller volumes (as small as 100 fL) and positioned on the surface using the manipulator.

20 **[00121]** Nanoribbon and nanowire sizes were determined with a scanning electron microscope (SEM).

[00122] FIG. 17 and FIG. 18 document several experiments that were performed with a single nanoribbon in various combinations with GaN and ZnO nanowires.

25 **[00123]** FIG. 17 illustrates the routing of GaN PL and lasing emission. FIG. 17A is a dark-field optical image of a coupled GaN nanowire 50 and SnO_2 nanoribbon 52. The label A denotes the location of the junction. FIG. 17B shows direct excitation of the SnO_2 nanoribbon at location B generates white PL that is guided to the ends of the SnO_2 cavity. Some of the light is scattered by a large particle found at C. The inset in FIG. 17B is a magnified view of the bottom emission spot. FIG. 17C is a magnified view of the junction area. The inset in FIG. 17C is a SEM image showing that the two structures

30

are staggered over 9 μm and touch for approximately 2 μm . FIG. 17D shows direct CW excitation of the GaN nanowire generates UV band-edge emission at 365 nm and a small amount of visible defect emission at 650 nm. The cavity is too thin to permit the confinement of red light, but (Inset) a UV camera detects strong waveguiding of the UV PL. FIG. 17E is an optical image of the routing of UV laser pulses from nanowire to nanoribbon. Here, the GaN cavity was pumped above its lasing threshold by a pulsed 266 nm source (itself invisible to this detector). FIG. 17F shows spectra comparing the GaN PL and lasing emission before and after passage through the nanoribbon cavity. The broad pseudo-Gaussian spontaneous emission peak (top) is broken into a series of sharp modes during its transit through the nanoribbon (WG PL). Likewise, the lasing emission at moderate pump power, which shows multiple modes (GaN lasing), is severely modulated by the mode structure of the SnO_2 cavity (bottom). Spectra are normalized and offset for clarity.

[00124] As can be seen, FIG. 17A shows a GaN nanowire (130 nm by 65 μm) that has been coupled to a SnO_2 nanoribbon (240 nm by 260 nm by 460 μm) with the micromanipulator. The magnified SEM view of the GaN- SnO_2 junction (Inset, FIG. 17B) indicates that the two structures are in physical contact over an interaction length of approximately 2 μm . This staggered-bonded configuration provides good optical coupling between the cavities and some degree of inter-wire adhesion (via electrostatic forces), which aids in the construction of multi-wire networks. Butt-end coupling is also effective, and it is possible for us to detect the transfer of light between nanowire cavities that are weakly coupled across an air gap of up to several hundred nanometers (not shown). If two nanoribbons are crossed instead of staggered, the coupling losses decrease with shallower intersection angles, which has also been observed recently for crossed CdS nanowires.

[00125] To demonstrate the routing of continuous wave light, we excited the GaN nanowire with the focused beam of a HeCd laser operating at 325 nm. Band-edge PL from the GaN cavity was channeled through the SnO_2 nanoribbon to emerge primarily at its far end. A fraction of the light was also

scattered by imperfections along the length of the nanoribbon (i.e., attached particles or macroscopic step edges). Far-field spectra collected from the output end of the nanoribbon (FIG. 17F) show that the quasi-Gaussian PL band of GaN is imprinted with the mode structure of the SnO₂ cavity during its transit. This mode structure is not longitudinal (Fabry-Perot) in nature, as it is for shorter nanowires; instead, it is a complex interference pattern dependent on nanoribbon shape and cross-sectional dimensions, among other factors.

[00126] Moreover, referring also to FIG. 18, it is possible to simultaneously guide the output of two (or more) nanolasers by coupling multiple ZnO and GaN nanowires to the same nanoribbon, opening up the possibility of performing nonlinear wave mixing within single nanocavities. FIG. 18A is a dark-field image of a GaN nanowire 54 and a ZnO nanowire 56 coupled to the same nanoribbon 58. The scale bar is 10 μm . FIG. 18B shows the spectrum of guided light collected at the far end of the nanoribbon when both nanowires were pumped above their lasing thresholds by the same train of optical pulses. The nanoribbon is the same used in FIG. 13 and FIG. 17.

[00127] Note that in contrast to their continuous wave emission, the pulsed emission of ZnO and GaN is nearly devoid of visible PL since the defect bands experience no gain. This is experimental verification that coherent optical pulses can be transferred between nanowires and steered hundreds of micrometers from their source. With high frequency electrical pumping, nanowire laser/waveguide combinations could be used to transduce and shuttle packets of electro-optical information within future computing and communications devices.

[00128] FIG. 19 illustrates GaN nanowire lasing. FIG. 19A shows a series of emission spectra at different pump fluence for an isolated GaN nanowire with a diameter of 150 nm and length of 45 μm . The inset in FIG. 19A shows the PL spectrum. FIG. 19B shows the energy curve for the same nanowire. Typical thresholds for GaN NW lasing were 5 μJ to 15 $\mu\text{J cm}^{-2}$. The inset in FIG. 19B is an image of lasing emission from a different GaN nanowire, showing its pronounced spatial pattern. By pumping the GaN nanowire above its lasing threshold ($\sim 5 \mu\text{J/cm}^2$) with pulsed UV excitation, we were able to

send single optical pulses from the nanowire laser through the nanoribbon waveguide (FIG. 17E). The spectrum of several thousand accumulated pulses (FIG. 17F) shows a series of sharp modes (FWHM = 0.8 nm) slightly red-shifted from the band edge of GaN. These are the Fabry-Perot type lasing modes of the GaN nanowire resonator, modulated in intensity by the nanoribbon cavity. We have obtained similar results with junctions between nanoribbons and lasing ZnO nanowires.

[00129] Referring now to FIG. 20 and FIG. 21, since diffraction losses in a subwavelength cavity increase markedly with wavelength, a nanoribbon waveguide preferentially confines the bluer portion of any non-monochromatic beam. As a result, nanoribbons act as short-pass filters with cutoff wavelengths that are determined by their cross-sectional dimensions and overall length.

[00130] FIG. 20 shows color filtering in a nanoribbon network 60. FIG. 20A is a dark-field image of a four-ribbon assembly as it guides white PL generated at the pump spot (left) and separates it into a different color at the end of each nanoribbon (right). The scale bar is 50 μm . FIG. 20B is a magnified view of the emission region. The branch nanoribbons 1-3 in FIG. 20B emitted green, aqua and blue light because of their progressively smaller cross-sections (350 nm by 140 nm, 260 nm by 175 nm and 210 nm by 135 nm, respectively). Their 50% cutoff wavelengths were determined by near-field scanning optical microscopy (NSOM) to be 543 nm, 502 nm and 478 nm. The stem nanoribbon is 260 nm by 240 nm by 390 μm . FIG. 20C shows that non-resonant blue light is transmitted to the end of all four nanoribbons, while FIG. 20D shows that green light is much more strongly guided by nanoribbon 1 than by nanoribbon 3 and FIG. 20E shows that red light is filtered out by all three branches. The scale bar is 20 μm .

[00131] As can be seen from FIG. 20, we assembled a simple network comprising four nanoribbons of different sizes to show how such a structure may be used to separate colors. When excited at 325 nm, the large nanoribbon that formed the stem of the network 60 emitted white light composed of two broad SnO_2 PL bands centered at 495 nm and 590 nm, as

can be seen from FIG. 21 which is a typical PL spectrum of a SnO₂ nanoribbon showing its two defect bands. Varying amounts of the stem emission then flows into the three shorter and consecutively thinner branch nanoribbons, separating the white light into green, aqua and blue components (ribbons 1-3). Alternatively, when monochromatic red light was launched into the stem only the stem nanoribbon lit up, while green light was guided strongly (weakly) by the largest (smallest) branch and blue light passed through all three branches as well as the stem (FIG. 20B-20D). Although this color filtering effect works only in short-pass mode, and so cannot, for instance, isolate the pure red component of a white beam, it may prove useful in such tasks as removing visible contamination from UV pulses or providing local excitation for fluorophores with narrow absorption bands, such as quantum dots.

[00132] Referring to FIG. 22, to test the limits of inter-cavity optical coupling, we assembled four nanoribbons into a rectangular grid (46 μm long by $\sim 25 \mu\text{m}$ wide) featuring X-junction vertices with small contact areas ($< 0.15 \mu\text{m}^2$) (FIG. 22A and Inset). FIG. 22A is a dark-field image of the four-ribbon structure, with the input channel extending off the frame to the right and the output channels labeled 1-7. The nanoribbons vary in size from 300-400 nm on a side. (FIG. 22A and Inset). A SEM image of the junction at the lower right vertex. FIG. 22B is a PL image as the input channel is pumped at 325 nm. Light is guided to the seven output ends with different intensities and colors as described below.

[00133] The structure was designed with one long channel for light input and seven short output channels that could be monitored simultaneously. As shown in FIG. 22B, direct excitation of the input channel triggered emission from all seven of the nanoribbon outputs, with the following intensity distribution: $1 \gg 6 > 4 \approx 7 > 3 > 5 > 2$. This is exactly the sequence one would expect after considering the trajectory of the incoming light and the intensity of scattering at the four nanoribbon-ribbon junctions. The light trajectory is important here since the low reflectivity of their end facets makes nanoribbons poor resonators (with an ideal finesse of ~ 1.3). As such, most photons do not

make multiple passes and light flow is highly directional. The right-angle intersections present significant obstacles to inter-cavity waveguiding by total internal reflection. At the same time, they act as quasi-isotropic scatterers that feed light between nanoribbons. Nanoribbon-to-ribbon losses, although
5 nearly maximized in this geometry, are still low enough for the activation of channels 2 and 3, which require photons to negotiate two right-angle junctions and transit three separate cavities. When we added a ZnO nanowire laser to the input channel and used it to launch light into the grid, emission was
10 detected from all channels but 2 and 3; the number of injected photons was simply too small to illuminate the parallel nanoribbon. Nanowire grids have already been employed to implement rudimentary electronic logic. Integrated optical logic and all-optical switches present exciting prospects, and our results show that grids of nanowires should be capable of routing signals for such tasks.

15 **[00134]** Due to their high refractive indices ($n \geq 2$), the nanoribbons and nanowires discussed here function well as waveguides in water and other liquids. This is a considerable advantage over subwavelength silica waveguides, which cannot efficiently confine visible light in liquids because of a low dielectric contrast ($n_{\text{silica}} \approx 1.45$). Waveguiding in liquids is especially
20 important for integrated on-chip chemical analysis and biological spectroscopy in which small excitation and detection volumes are required.

[00135] As can be seen, chemically synthesized nanoribbon and nanowire waveguides have two unique and potentially useful features for subwavelength photonics applications. First, nanowires push subwavelength
25 optical fibers beyond silica. The scores of materials that can now be made in nanowire form include active, passive, nonlinear and semiconducting inorganic crystals, as well as a wide variety of polymers. Simultaneous photon, charge carrier and spin manipulation is possible within and between nanowires of different compositions. Also, many of these materials have
30 higher refractive indices than silica-based glasses, permitting light of a given wavelength to be confined within thinner structures for denser integration. This enables waveguiding in liquids and makes it possible to extend

subwavelength guiding to telecommunications wavelengths using, for example, an approximately 300 nm diameter Si or GaP nanowires. Second, nanowires are freestanding, mechanically flexible elements that can be manipulated on surfaces or used as mobile probes in fluids. As such, they offer a type of versatility difficult to achieve with lithographically-defined structures that are permanently affixed to their substrates.

[00136] The disadvantages of nanowire photonics include (i) the paucity of parallel assembly methods for accurately arranging large groups of nanowires into useful structures; (ii) relatively high inter-wire coupling losses compared to monolithic waveguides formed by lithography (coupling losses could be greatly reduced if branched, multi-component nanowires were developed to replace the staggered or crossed nanowire cavities used here); (iii) the lesser geometric perfection of nanowire assemblies relative to the precise shapes and sizes definable with lithography. Geometric imprecision introduces some uncertainty in the resulting light propagation and adds complexity to nanowire experiment/theory comparisons. However, despite these limitations, nanowires and their assemblies provide an important new platform for photonics studies and applications that is only beginning to be investigated.

[00137] It will be appreciated that the subwavelength waveguide described herein can be used as a functional element in photonic circuits such as optical networks, optical filters, optical directional couplers, emitter-waveguide-detector junctions, optical probes, optical sensors, optical routers, optical junctions, optical modulators, optical Y-junctions, optical branch networks, Mach-Zehnder interferometers, optical ring oscillators, nanolasers, optical phase shifters, fluidic sensors, fluidic probes, microfluidic devices, optical spectrometers, and optical crossbar grids. Those skilled in the art will also appreciate that the nanostructures described herein can be fabricated and incorporated into devices, systems and structures using various techniques known in the art. Additionally, reference is made to U.S. Patent No. 6,882,051, entitled "NANOWIRES, NANOSTRUCTURES AND DEVICES FABRICATED THEREFROM" issued on April 19, 2005, which is incorporated herein by reference in its entirety, and to U.S. Patent Application Publication

No. US 2004/0131537 A1, entitled "FUNCTIONAL BIMORPH COMPOSITE NANOTAPES AND METHODS OF FABRICATION" published on July 8, 2004, also incorporated herein by reference in its entirety.

[00138] Although the description above contains many details, these should not
5 be construed as limiting the scope of the invention but as merely providing
illustrations of some of the presently preferred embodiments of this invention.
Therefore, it will be appreciated that the scope of the present invention fully
encompasses other embodiments which may become obvious to those skilled
in the art, and that the scope of the present invention is accordingly to be
10 limited by nothing other than the appended claims, in which reference to an
element in the singular is not intended to mean "one and only one" unless
explicitly so stated, but rather "one or more." All structural, chemical, and
functional equivalents to the elements of the above-described preferred
embodiment that are known to those of ordinary skill in the art are expressly
15 incorporated herein by reference and are intended to be encompassed by the
present claims. Moreover, it is not necessary for a device or method to
address each and every problem sought to be solved by the present invention,
for it to be encompassed by the present claims. Furthermore, no element,
component, or method step in the present disclosure is intended to be
20 dedicated to the public regardless of whether the element, component, or
method step is explicitly recited in the claims. No claim element herein is to
be construed under the provisions of 35 U.S.C. 112, sixth paragraph, unless
the element is expressly recited using the phrase "means for."

CLAIMS

What is claimed is:

1. A subwavelength optical waveguide, comprising:
5 a nanoribbon or nanowire having a diameter that is less than the wavelength of light to be guided.
2. An optical waveguide as recited in claim 1, wherein said nanoribbon or nanowire has an aspect ratio greater than approximately 1000.
- 10 3. An optical waveguide as recited in claim 1, wherein said nanoribbon or nanowire comprises SnO₂.
4. An optical waveguide as recited in claim 1, wherein said nanoribbon or
15 nanowire comprises ZnO.
5. An optical waveguide as recited in claim 1, wherein said nanoribbon or nanowire has a diameter ranging from approximately 100 nm to approximately 400 nm.
- 20 6. An optical waveguide as recited in claim 1, wherein visible photoluminescence (PL) emission is guidable through said waveguide.
7. An optical waveguide as recited in claim 1, wherein said nanoribbon or
25 nanowire has a length of up to approximately 5000 μm .
8. An optical waveguide as recited in claim 1, wherein said nanoribbon or nanowire has a substantially uniform rectangular cross-section.
- 30 9. An optical waveguide as recited in claim 1, wherein said nanoribbon or nanowire has a substantially rectangular cross section ranging from approximately 15 nm x 5 nm to approximately 2 μm x 1 μm .

10. An optical waveguide as recited in claim 1, wherein said nanoribbon or nanowire has a cross-section ranging from approximately 100 nm x 100 nm to approximately 400 nm x 400 nm.

5

11. An optical waveguide as recited in claim 10, wherein said waveguide functions to steer visible and ultraviolet light in a subwavelength cavity.

12. An optical waveguide as recited in claim 1, wherein said waveguide
10 functions as a waveguide of internally generated photoluminescence (PL) and nonresonant UV/visible light emitted from an adjacent, evanescently coupled, nanoribbon, nanowire or external laser diode.

13. An optical waveguide as recited in claim 1, wherein said waveguide
15 comprises a single-crystalline structure that is manipulatable and positionable on a substrate surface.

14. An optical waveguide as recited in claim 13, wherein said substrate
surfaces comprising SiO₂ and mica substrate surfaces.

20

15. An optical waveguide as recited in claim 1, wherein bending said nanoribbon or nanowire changes output light mode structure.

16. An optical waveguide as recited in claim 1, wherein said light is
25 guidable through said waveguide in liquid media.

17. An optical waveguide as recited in claim 16, wherein said waveguide is configured for integrated on-chip chemical analysis or biological spectroscopy in which small excitation and detection volumes are required.

30

18. An optical waveguide as recited in claim 16, wherein said waveguide is configured for probing molecules in a fluorescence, absorption or surface-enhanced

Raman scattering (SERS) scheme using decaying light field outside of the waveguide to induce photon absorption or scattering.

19. An optical waveguide as recited in claim 1, wherein said waveguide is a
5 functional element in a photonic circuit consisting essentially of optical networks,
optical filters, optical directional couplers, emitter-waveguide-detector junctions,
optical probes, optical sensors, optical routers, optical junctions, optical modulators,
optical Y-junctions, optical branch networks, Mach-Zehnder interferometers, optical
ring oscillators, nanolasers, optical phase shifters, fluidic sensors, fluidic probes,
10 microfluidic devices, optical spectrometers, and optical crossbar grids.

20. An optical waveguide as recited in claim 19, wherein a said filter
comprises a short-pass filter with a tunable cutoff based on path length.

15 21. An optical waveguide as recited in claim 19, wherein a said optical
coupler comprises a hetero-junction created between a single ZnO nanowire and a
SnO₂ nanoribbon.

22. An optical waveguide as recited in claim 19, wherein a said optical
20 junction comprises a SnO₂/SnO₂ junction formed by coupling two nanoribbon
waveguides at end facets.

23. An optical waveguide as recited in claim 19, wherein a said optical
crossbar grid comprises two pairs of orthogonal said optical waveguides that conduct
25 light through abrupt 90° angles.

24. A subwavelength optical waveguide, comprising:
a nanoribbon or nanowire having a diameter that is less than the wavelength
of light to be guided;
30 wherein said nanoribbon or nanowire has an aspect ratio greater than
approximately 1000.

25. A subwavelength optical waveguide, comprising:

a nanoribbon or nanowire having a diameter that is less than the wavelength of light to be guided;

wherein said waveguide is a functional element in a photonic circuit consisting essentially of optical networks, optical filters, optical directional couplers, emitter-waveguide-detector junctions, optical probes, optical sensors, optical routers, optical junctions, optical modulators, optical Y-junctions, optical branch networks, Mach-Zehnder interferometers, optical ring oscillators, nanolasers, optical phase shifters, fluidic sensors, fluidic probes, microfluidic devices, optical spectrometers, and optical crossbar grids.

26. A subwavelength optical waveguide, comprising:

a nanoribbon or nanowire having a diameter that is less than the wavelength of light to be guided;

wherein said nanoribbon or nanowire has an aspect ratio greater than approximately 1000; and

wherein said nanoribbon or nanowire has a substantially rectangular cross-section ranging from approximately 15 nm x 5 nm to approximately 2 μm x 1 μm .

27. An optical waveguide as recited in claim 26, wherein said nanoribbon or nanowire has a cross-section ranging from approximately 100 nm x 100 nm to approximately 400 nm x 400 nm.

1/32

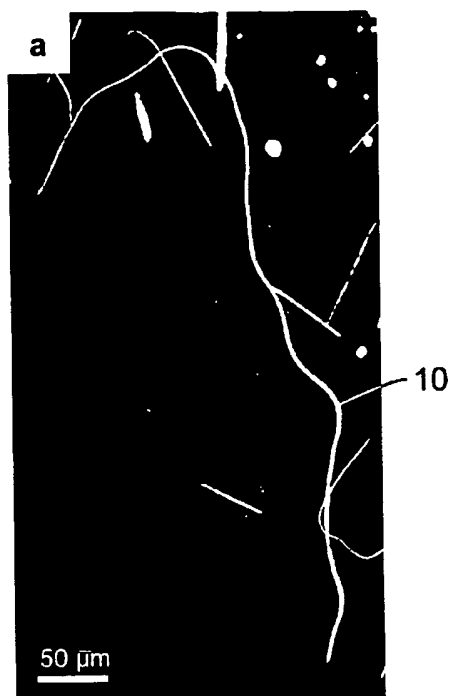


FIG. 1A

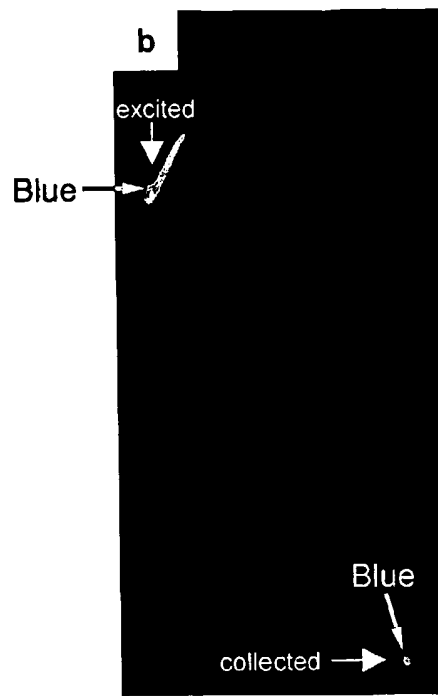


FIG. 1B

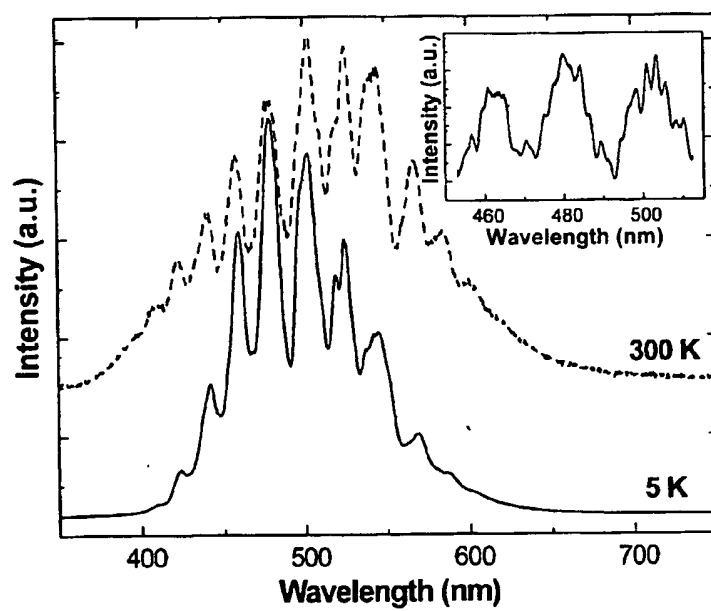


FIG. 1C

2/32

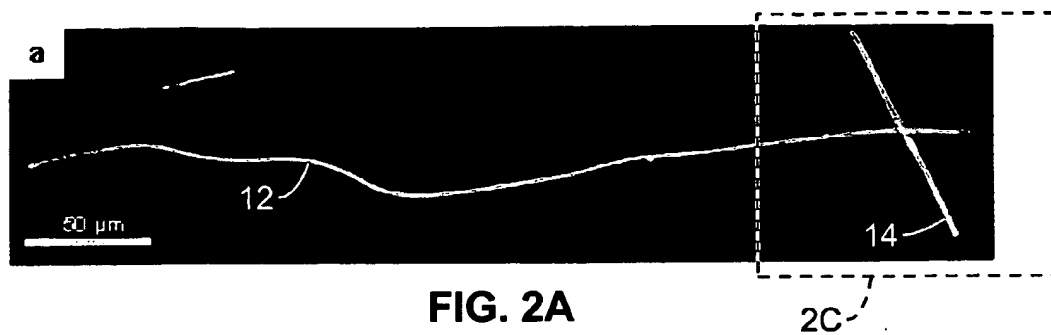


FIG. 2A



FIG. 2B

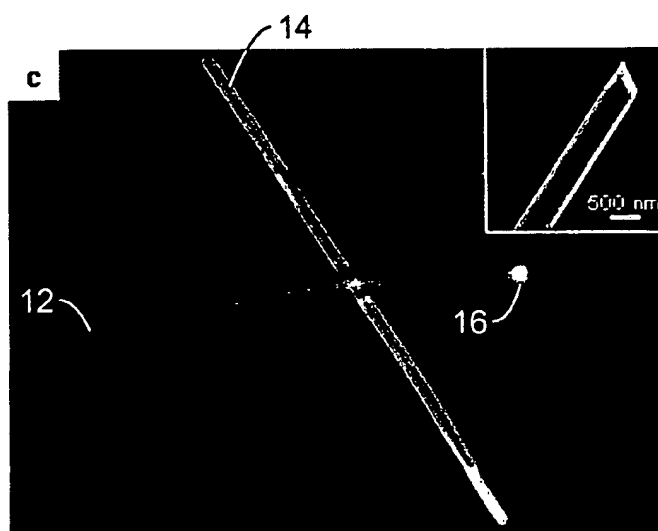


FIG. 2C

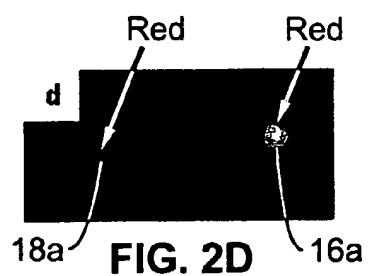


FIG. 2D

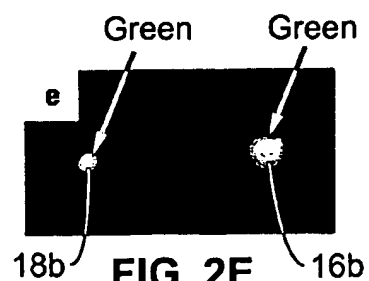


FIG. 2E

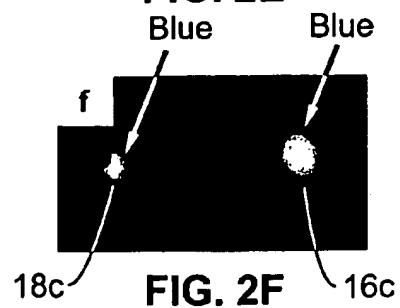


FIG. 2F

3/32

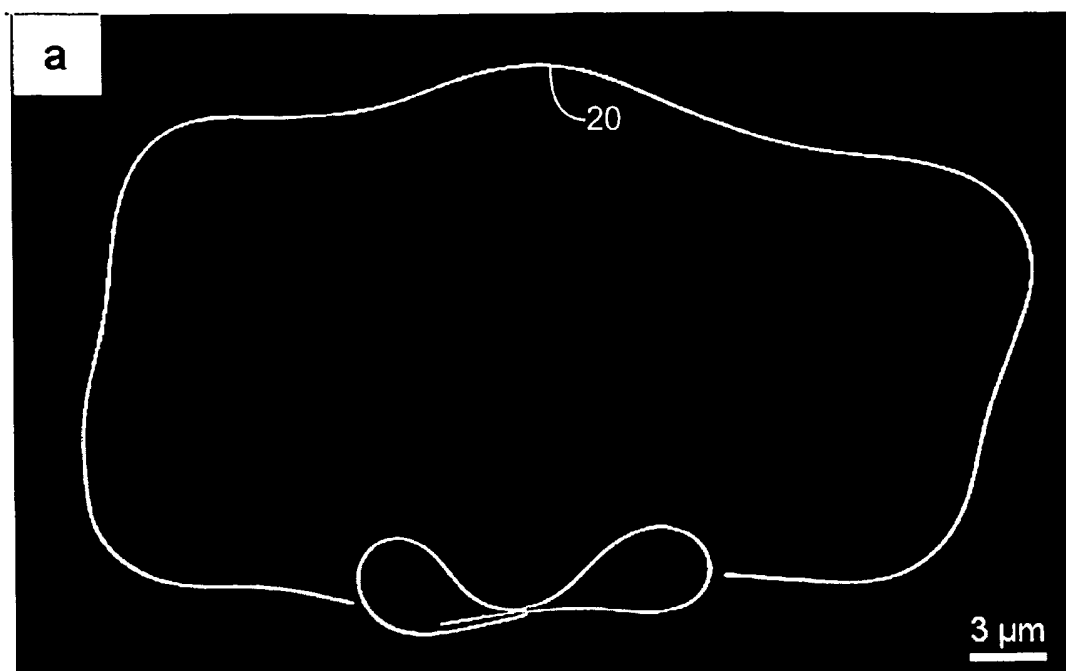


FIG. 3A

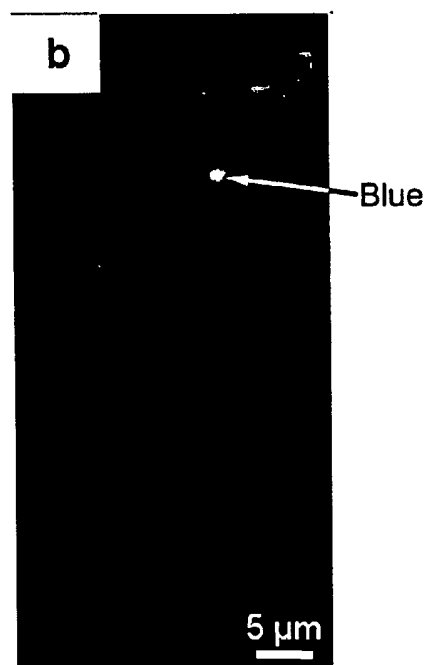


FIG. 3B

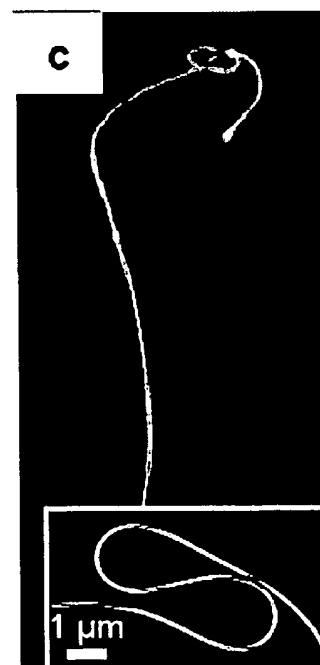


FIG. 3C

4/32



FIG. 3D



FIG. 3E



FIG. 3F

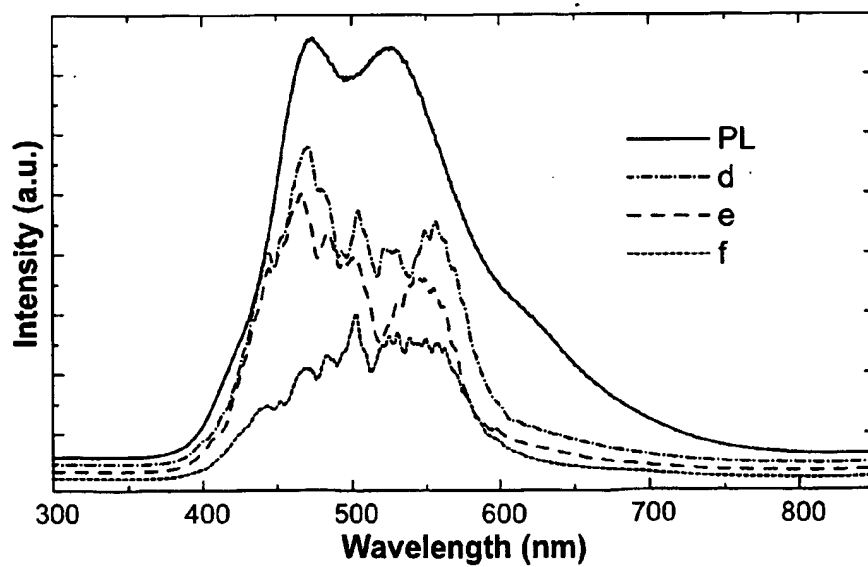


FIG. 3G

5/32

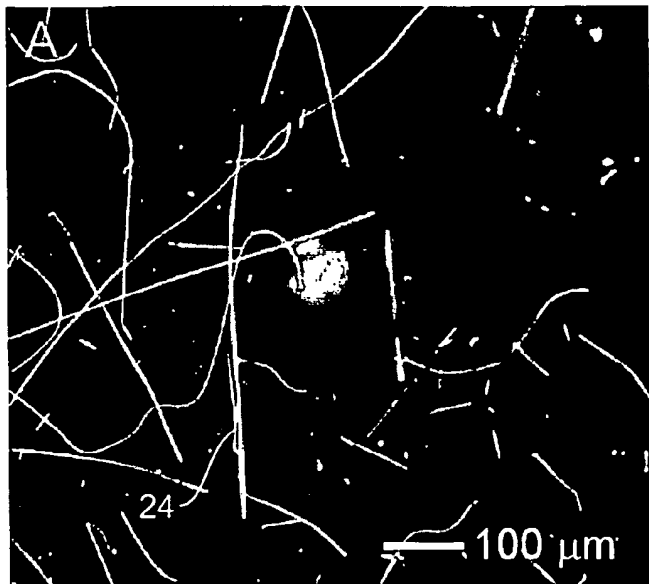


FIG. 4A



FIG. 4B

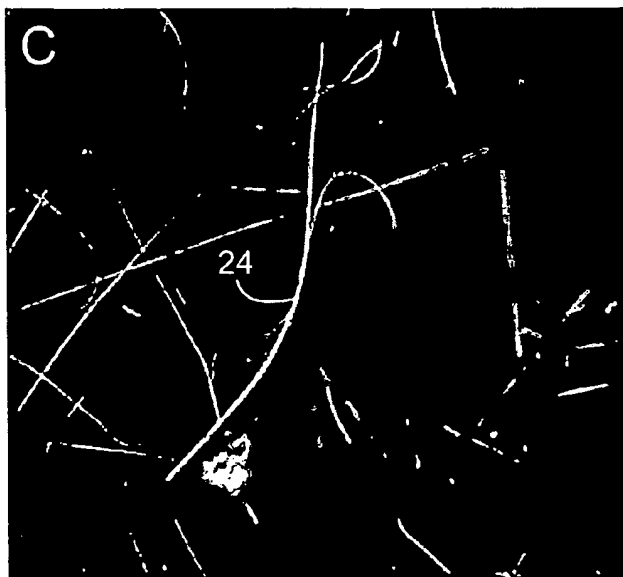


FIG. 4C

6/32

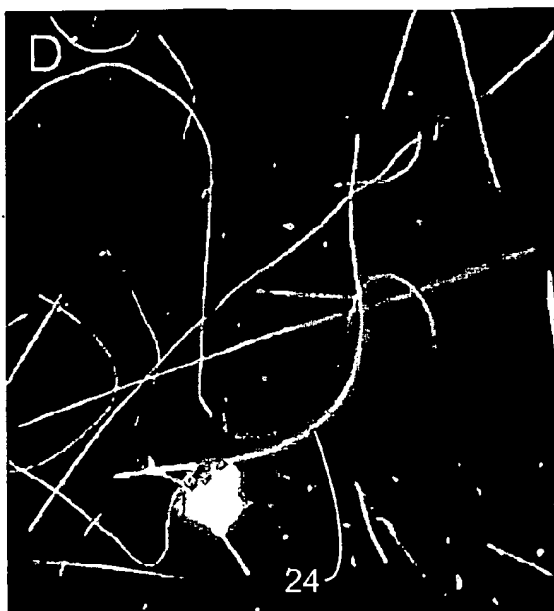


FIG. 4D

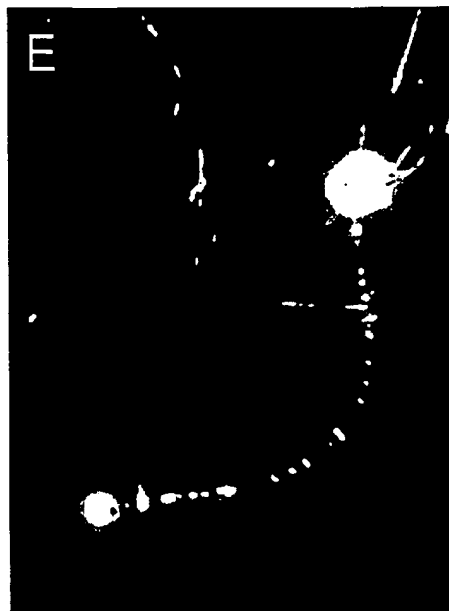


FIG. 4E

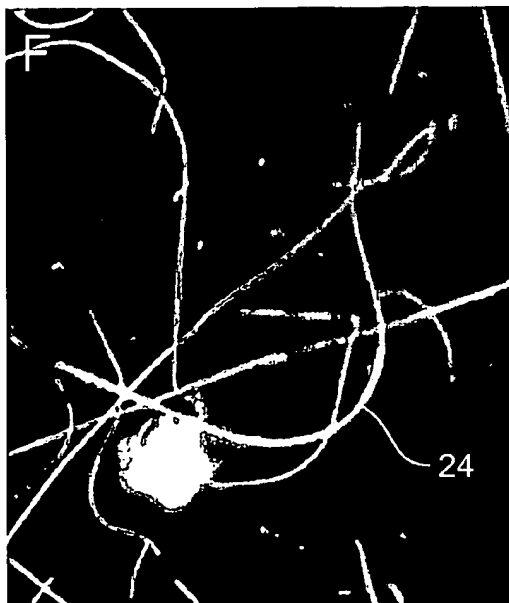


FIG. 4F

7/32

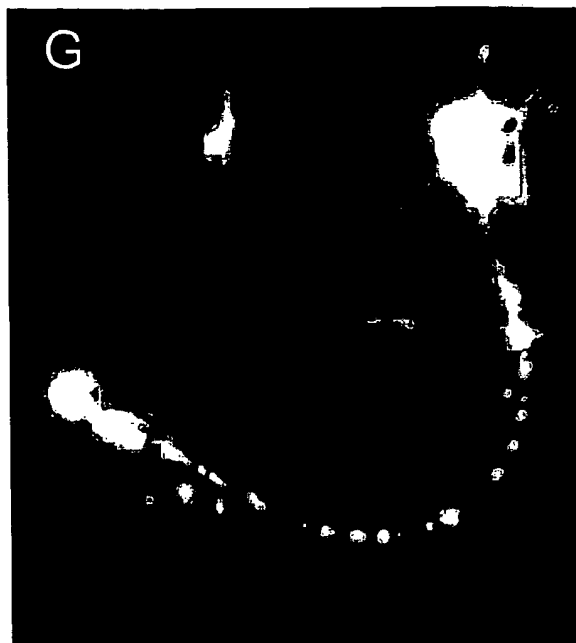


FIG. 4G

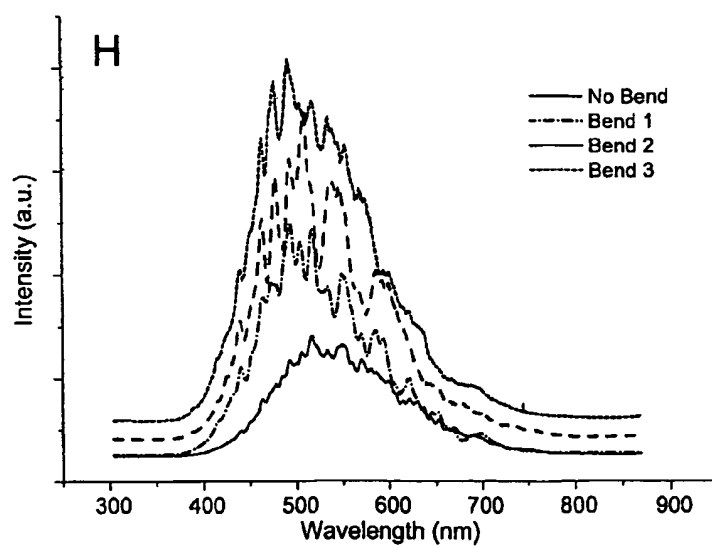


FIG. 4H

8/32

FIG. 5A

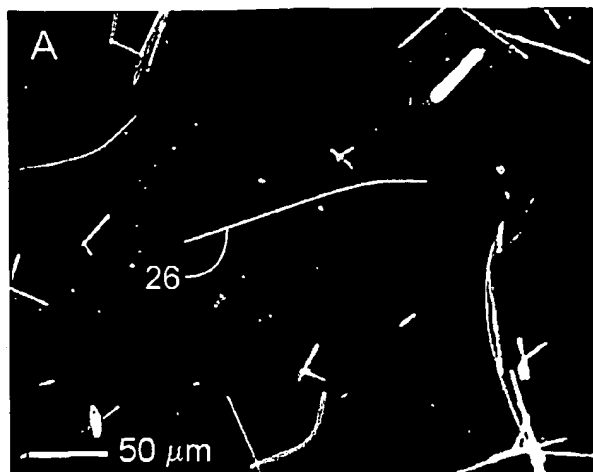
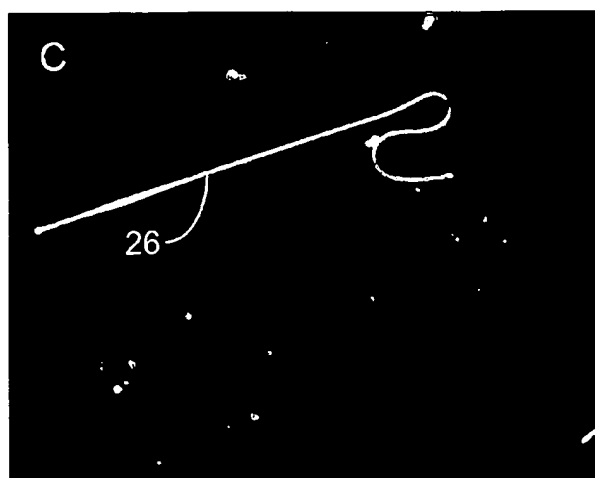


FIG. 5B



FIG. 5C



9/32

FIG. 5D



FIG. 5E

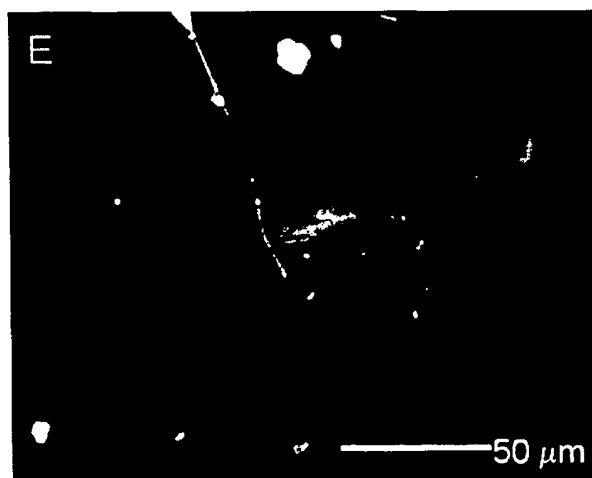
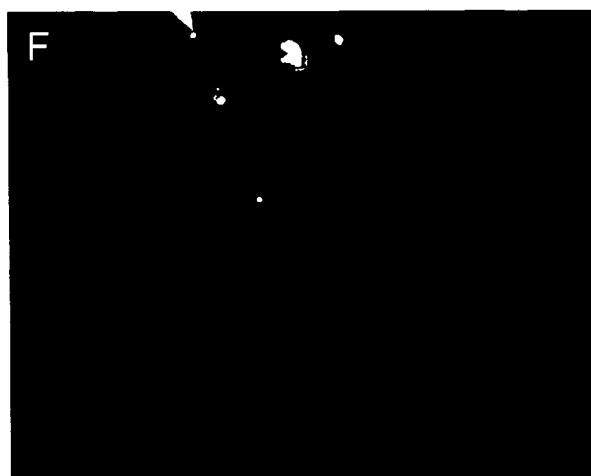


FIG. 5F



10/32

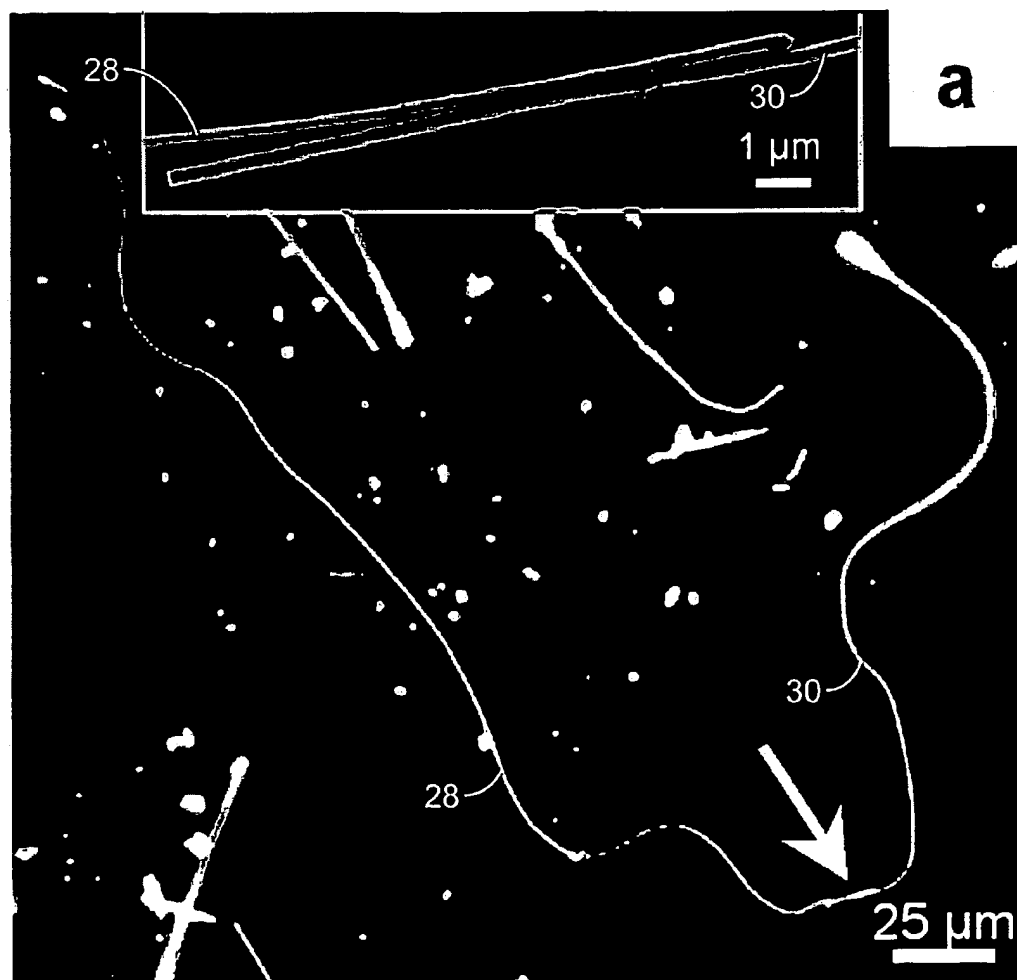


FIG. 6A

11/32

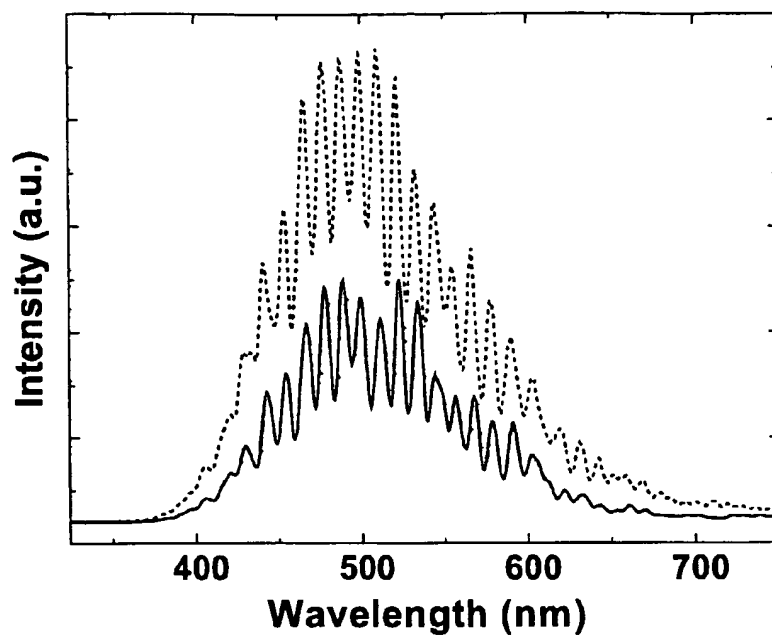


FIG. 6B

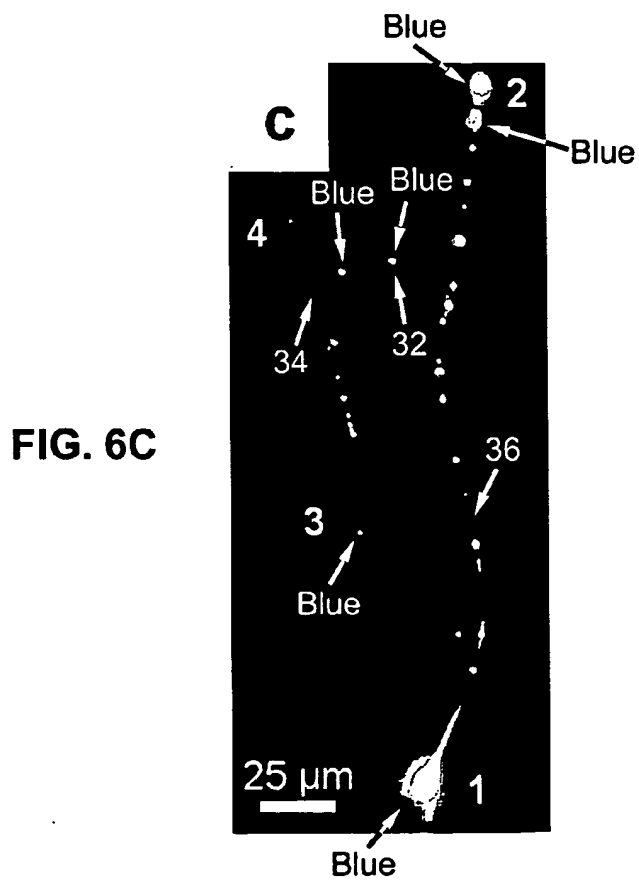


FIG. 6C

12/32

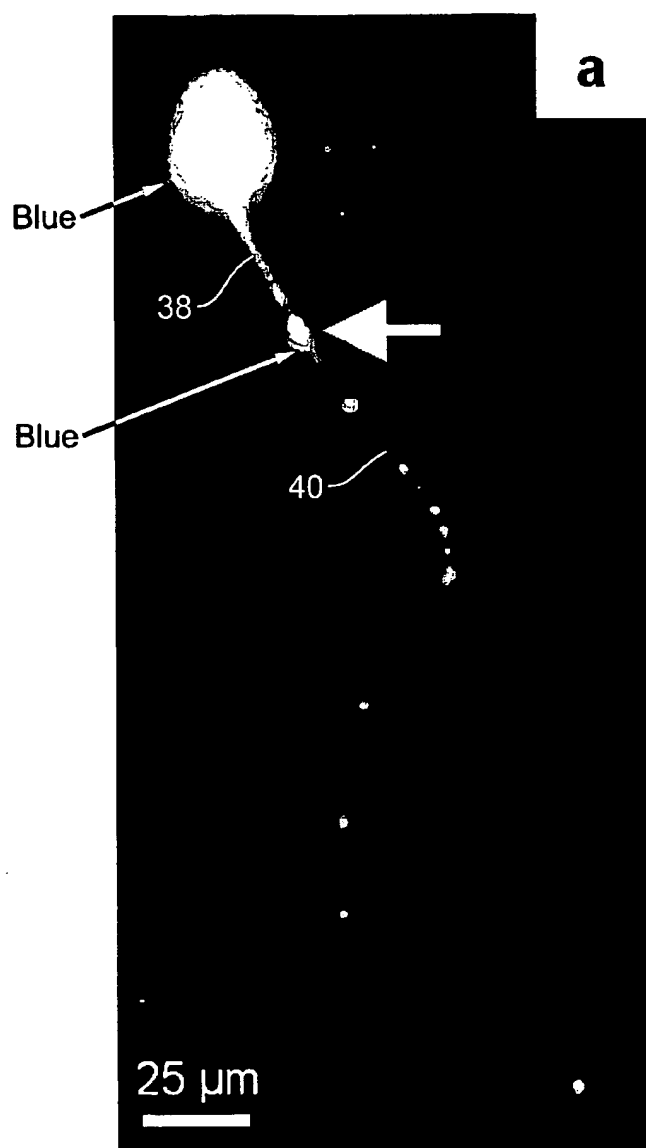


FIG. 7A

13/32

FIG. 7B

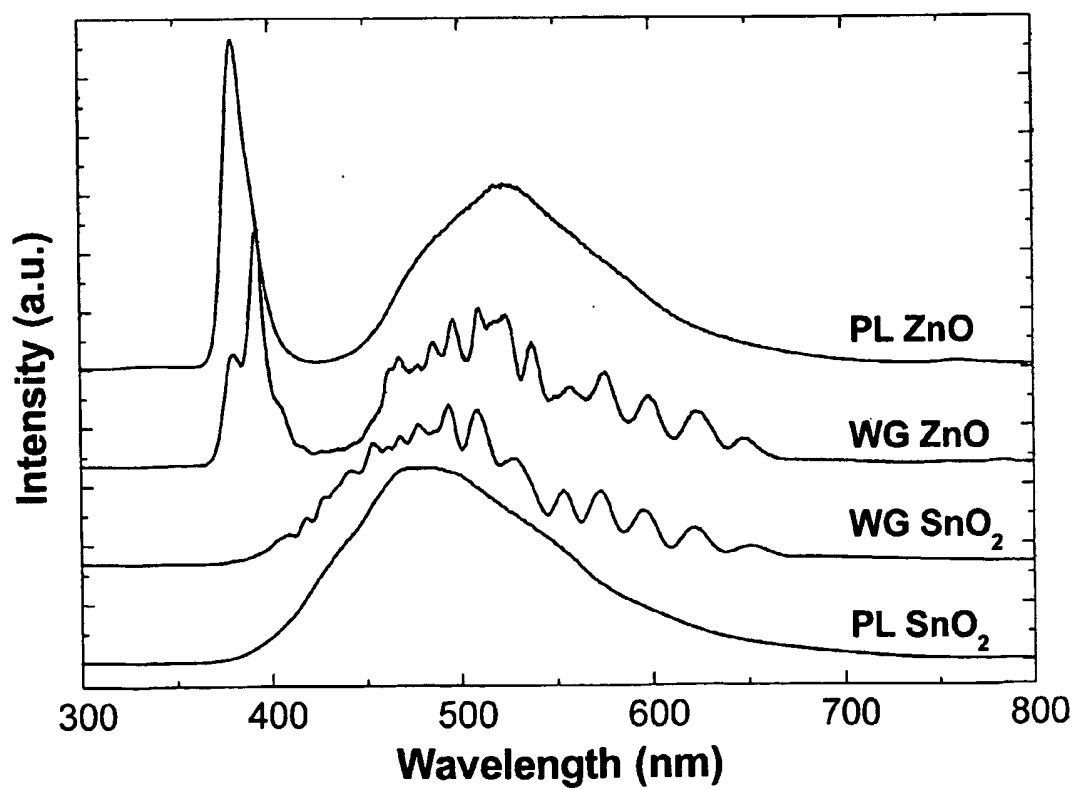
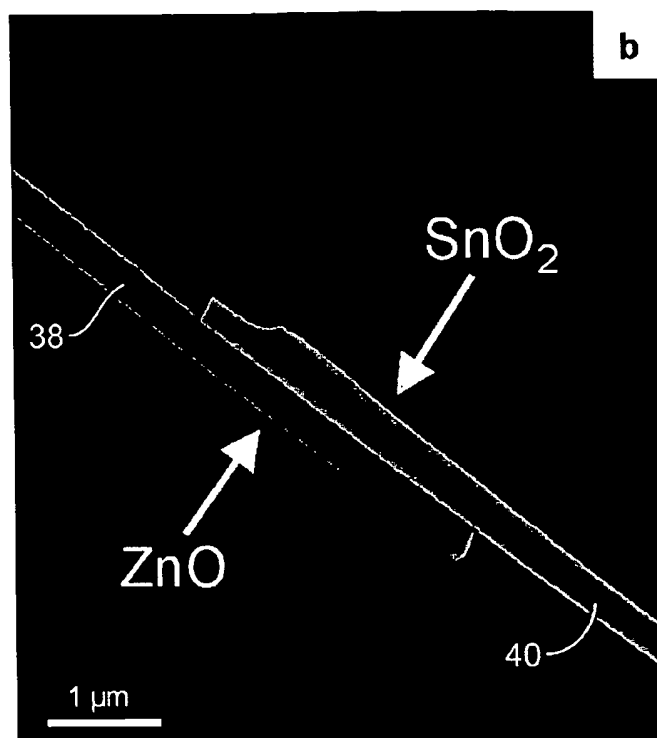
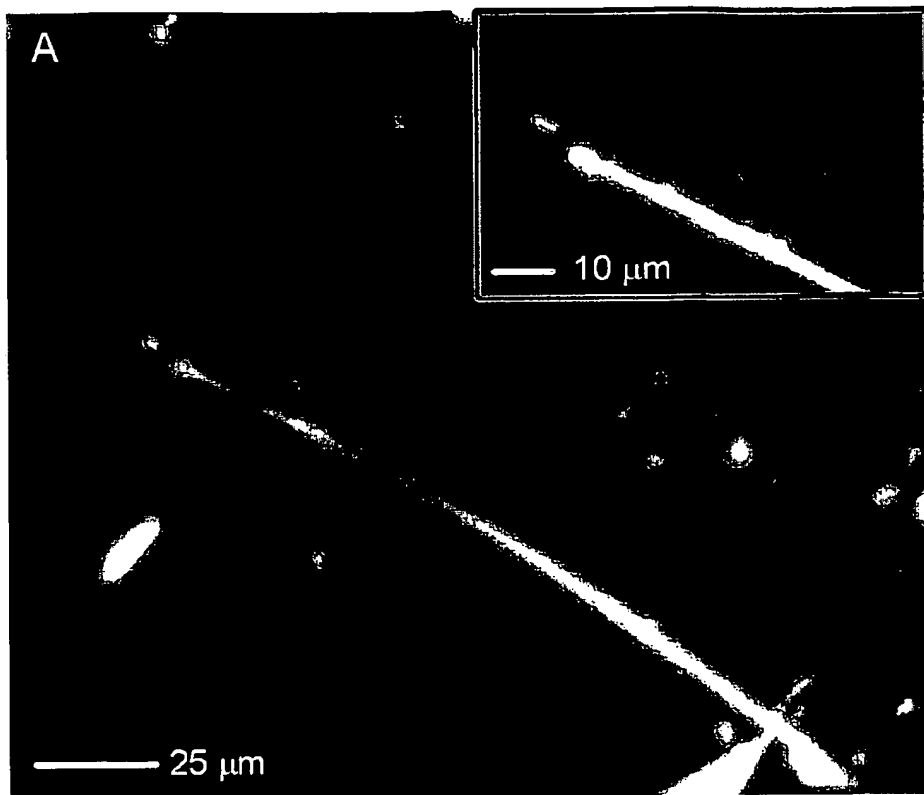
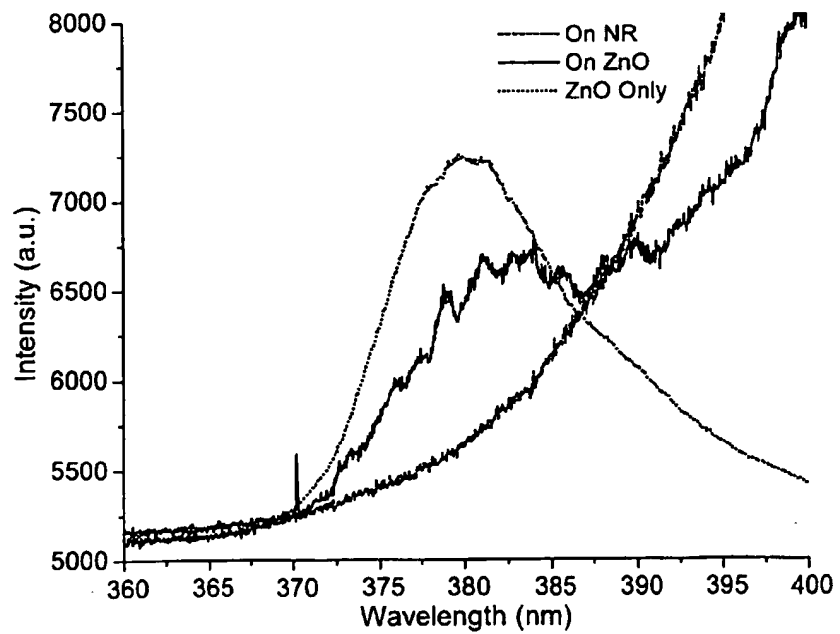


FIG. 7C

14/30

**FIG. 8A****FIG. 8B**

15/32

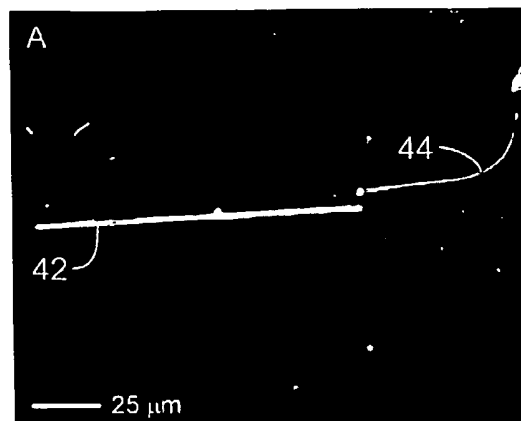


FIG. 9A

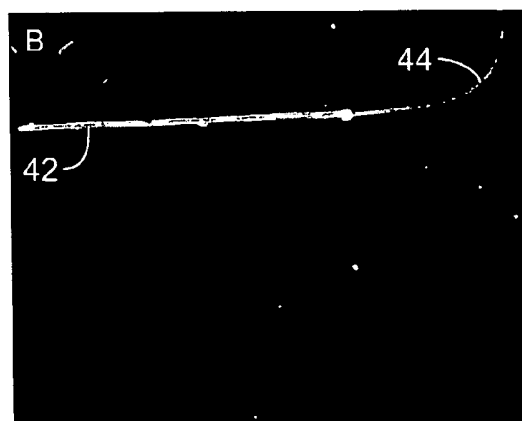


FIG. 9B

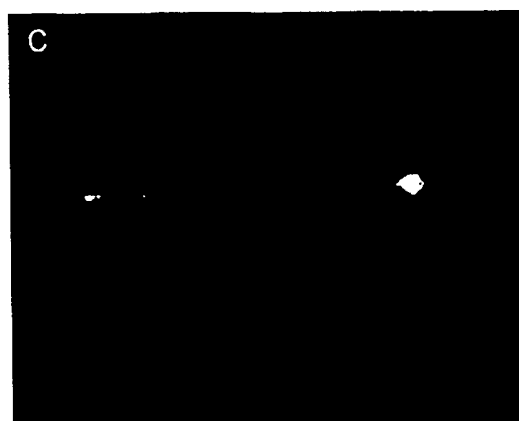


FIG. 9C

16/32

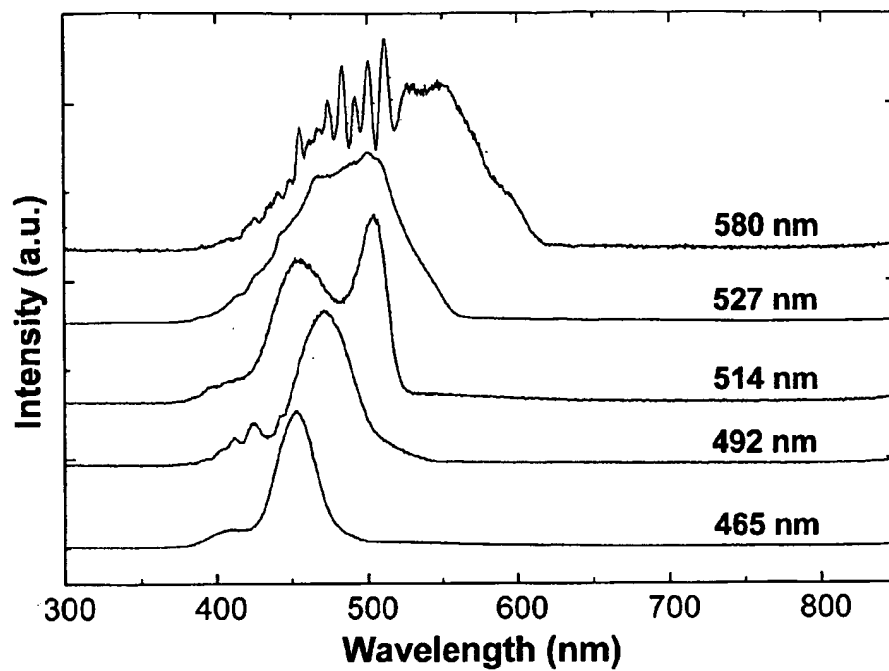


FIG. 10A

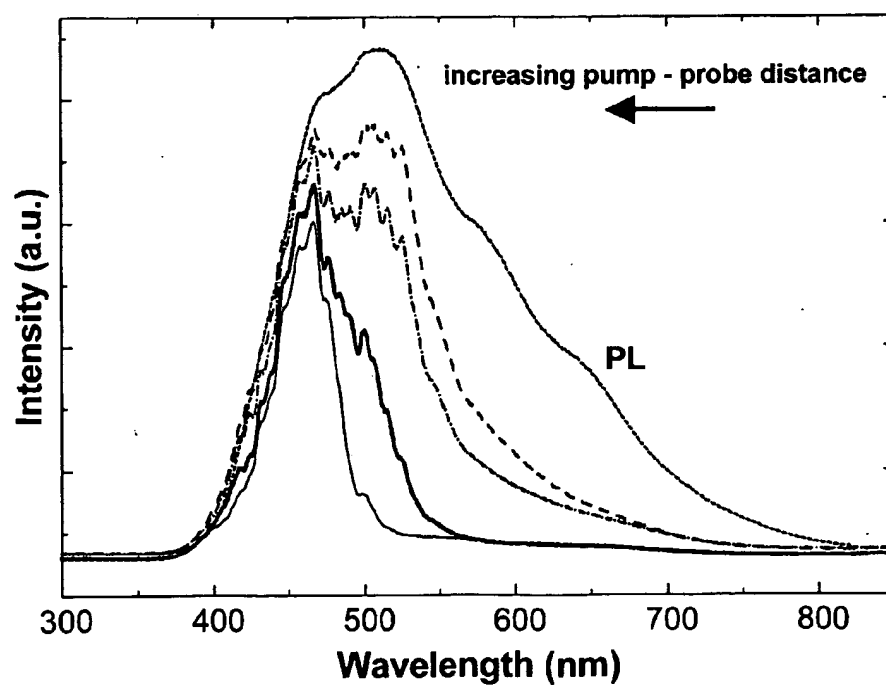


FIG. 10B

17/32

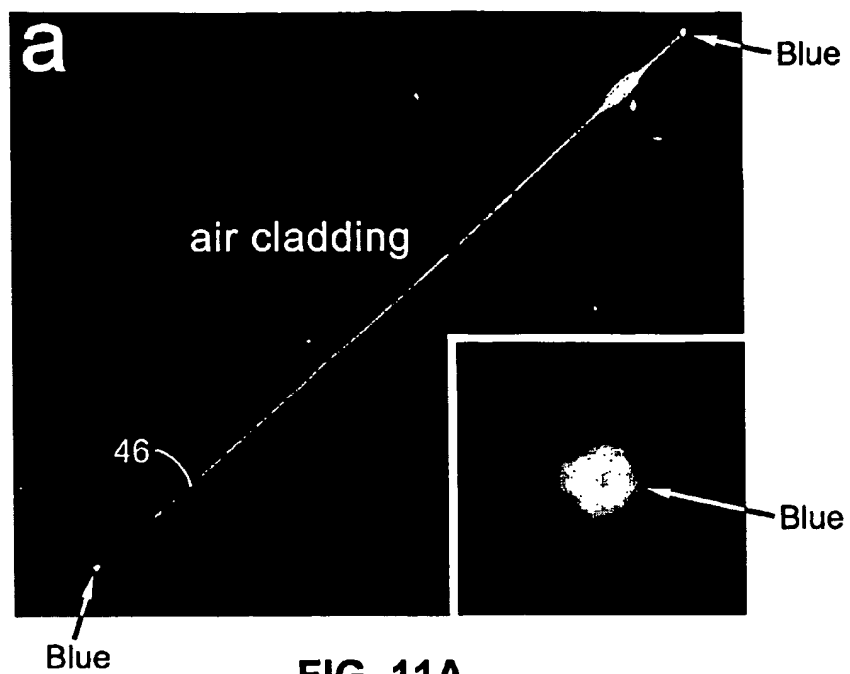


FIG. 11A

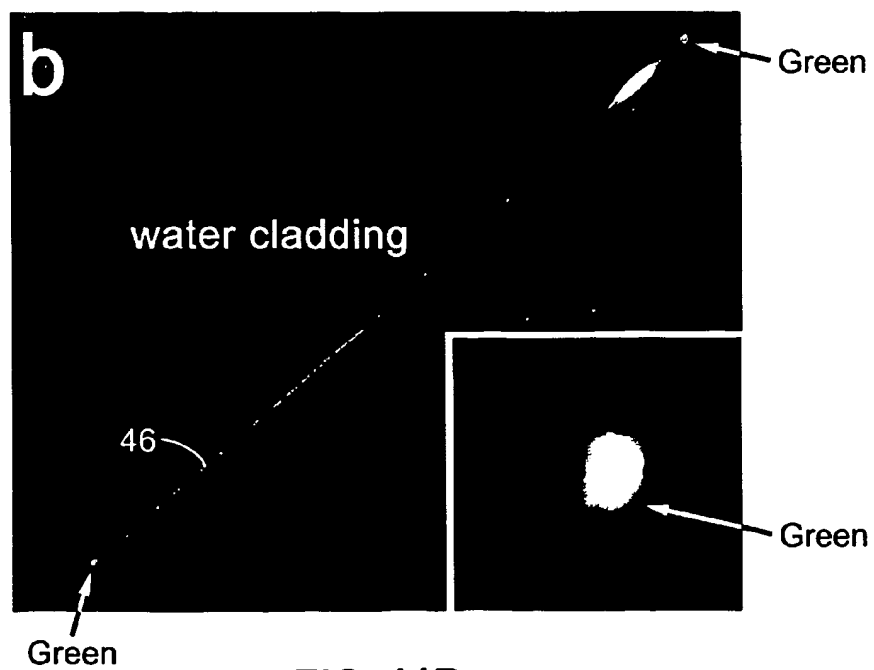


FIG. 11B

18/32

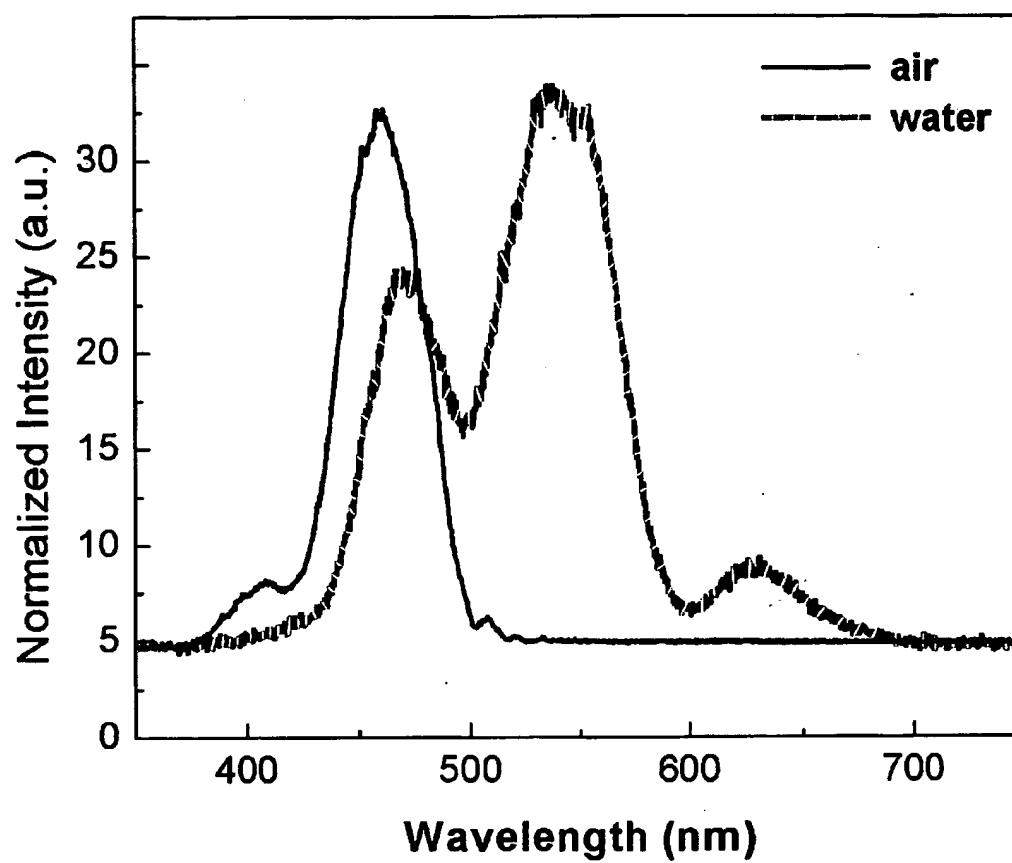


FIG. 11C

19/32

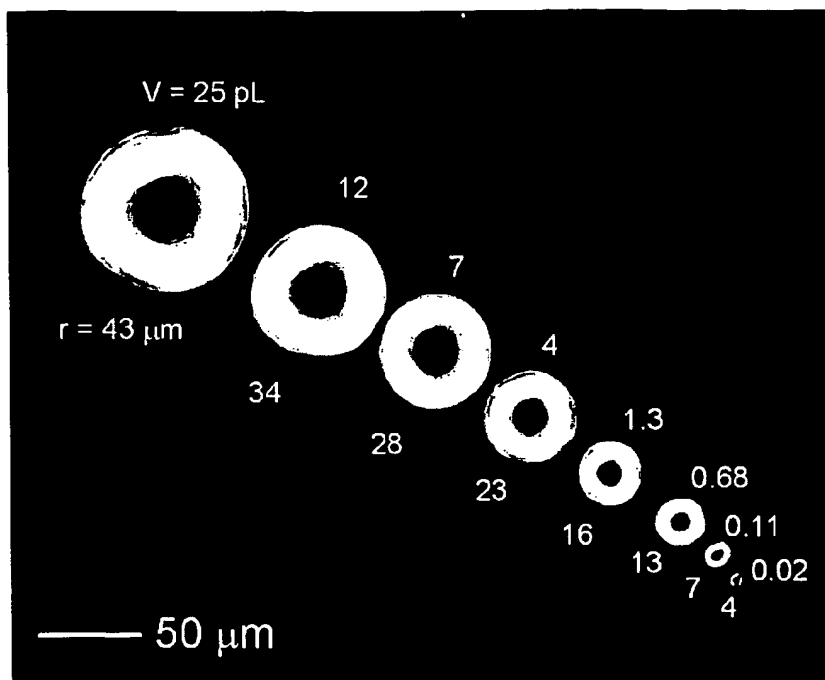


FIG. 12A

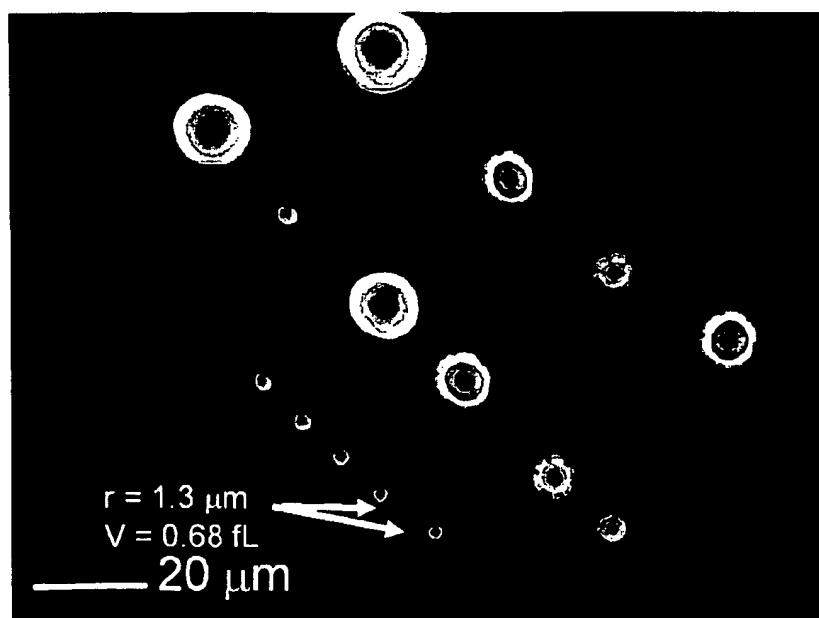


FIG. 12B

20/32

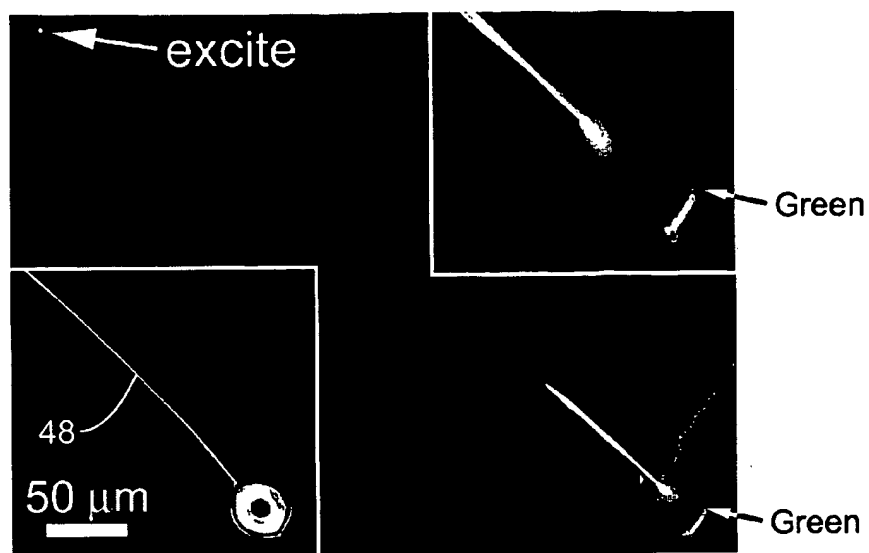


FIG. 13A

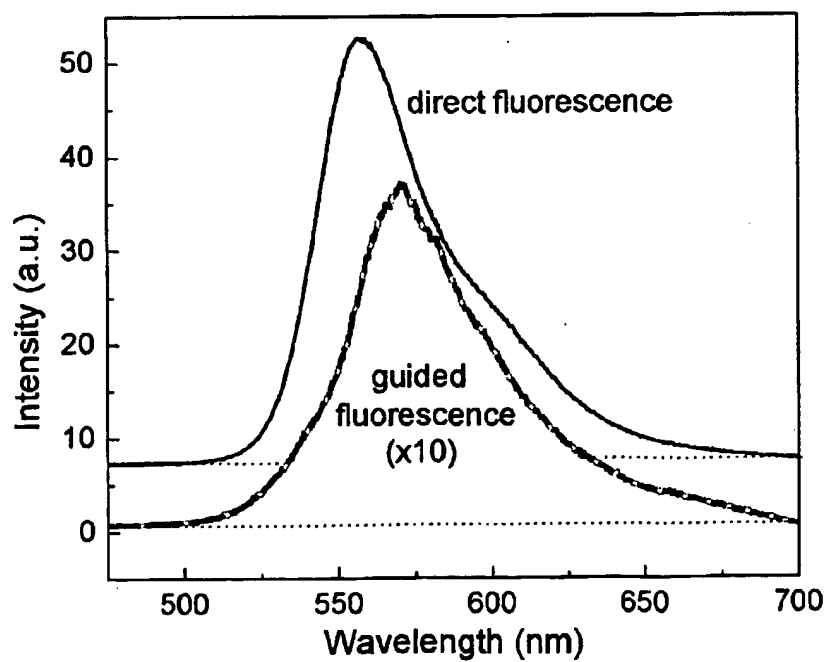


FIG. 13B

21/32

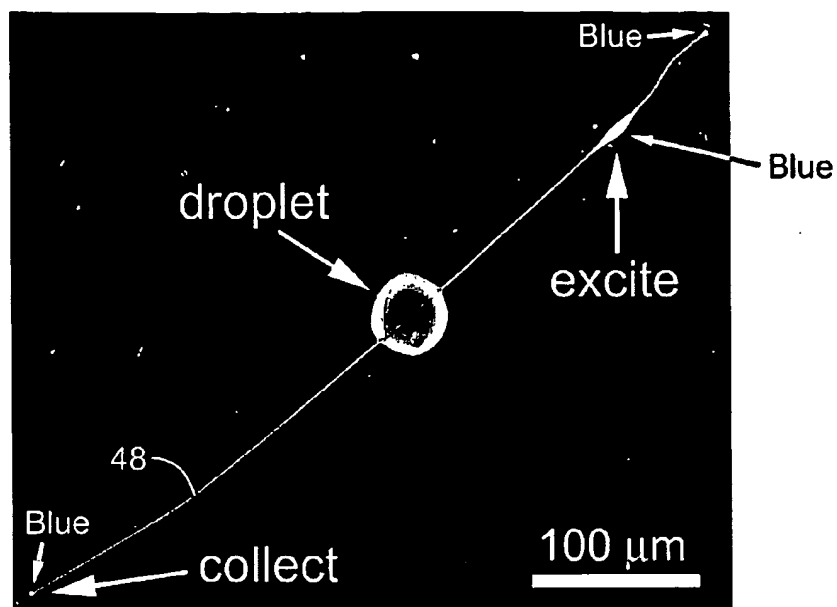


FIG. 13C

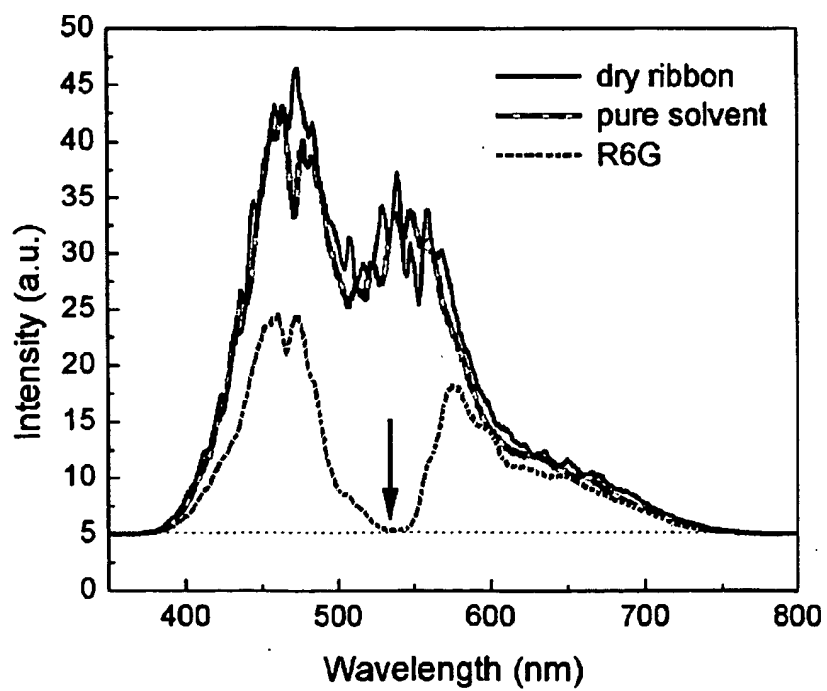


FIG. 13D

22/32

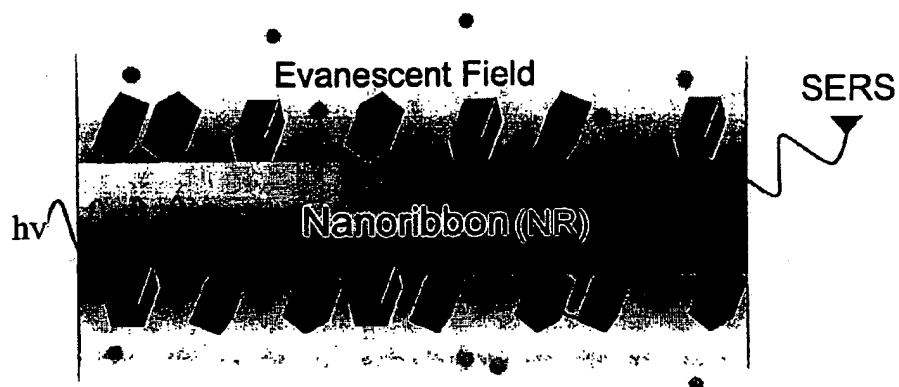


FIG. 14A

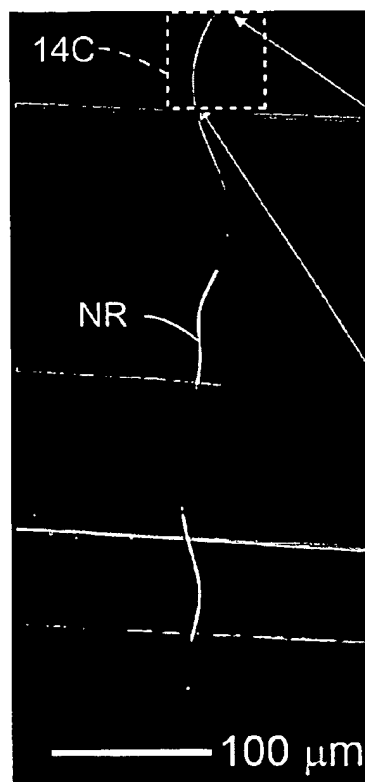


FIG. 14B

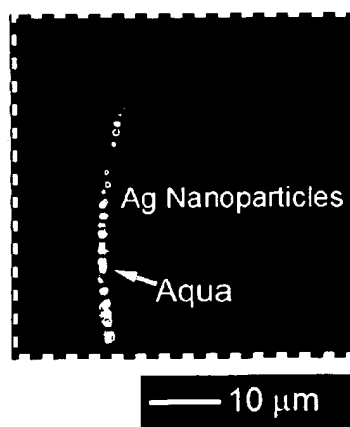


FIG. 14C

23/32

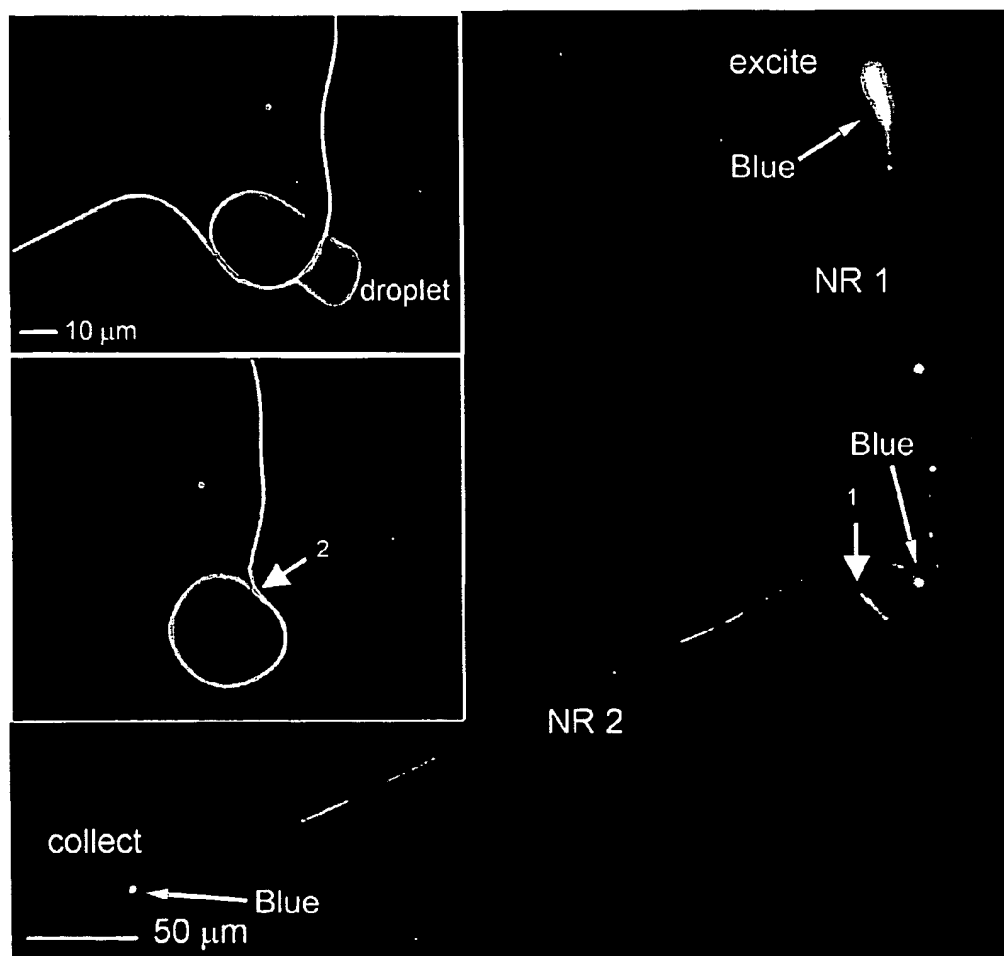
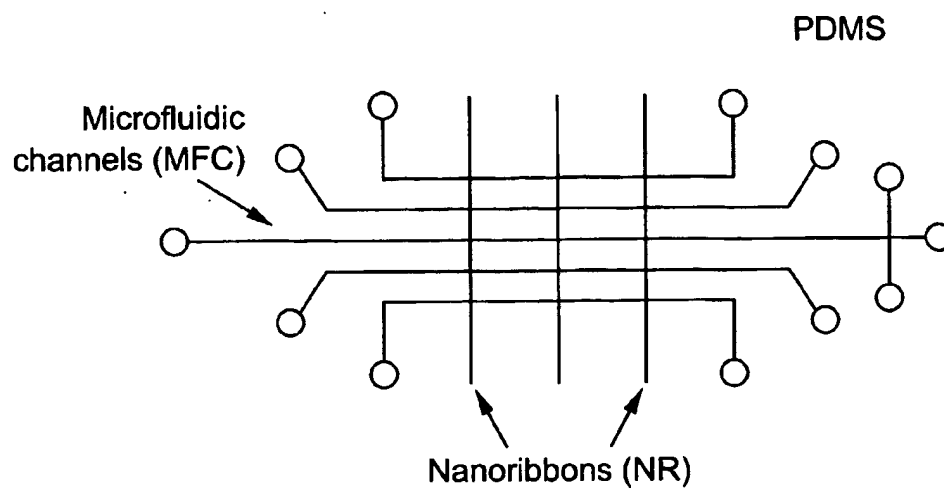
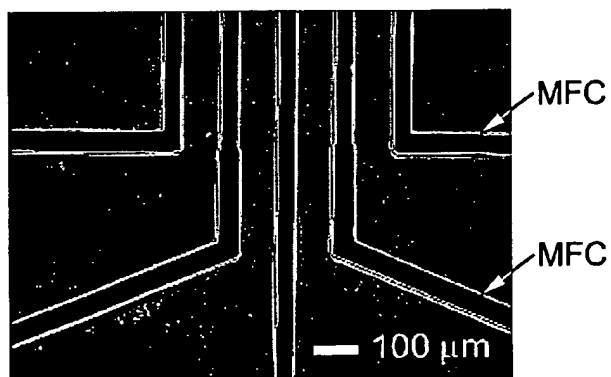
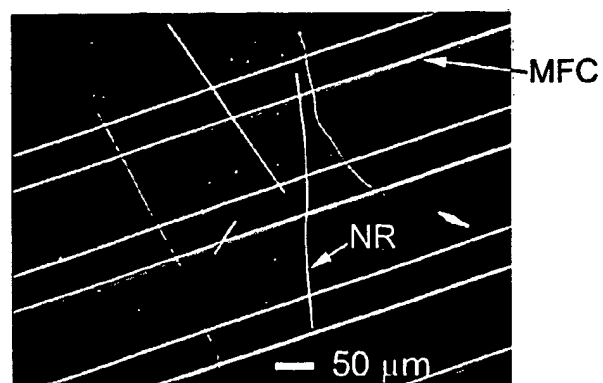


FIG. 15

24/32

**FIG. 16A****FIG. 16B****FIG. 16C**

25/32

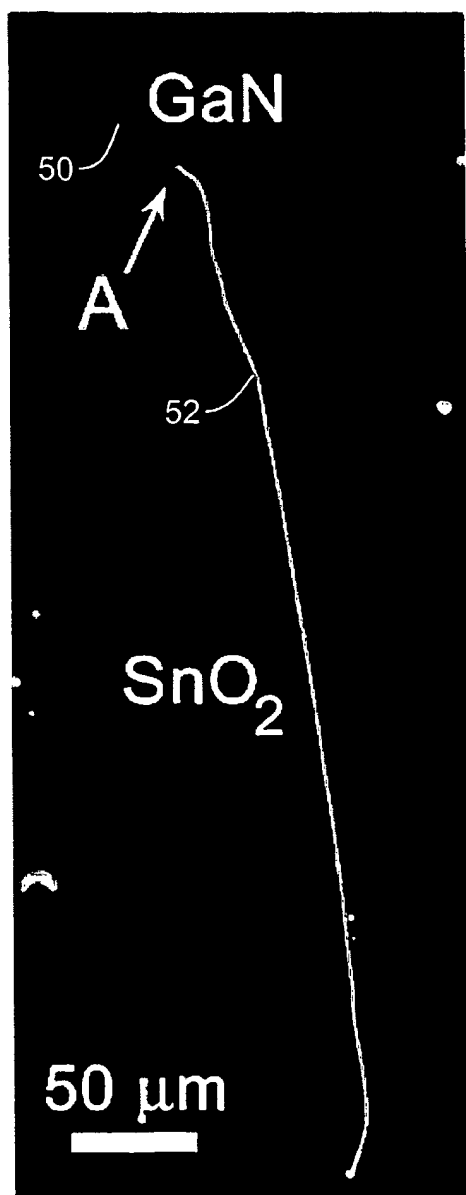


FIG. 17A

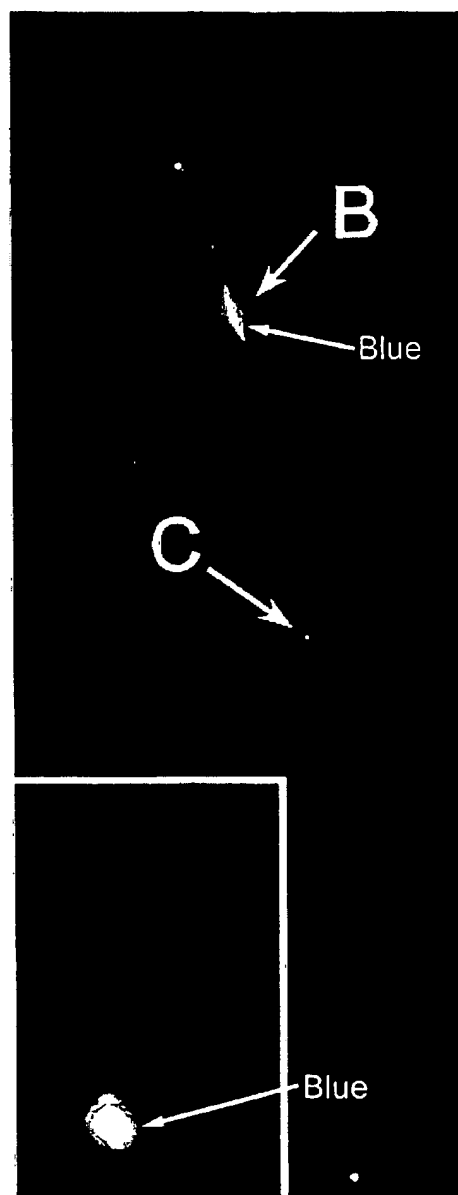


FIG. 17B

26/32

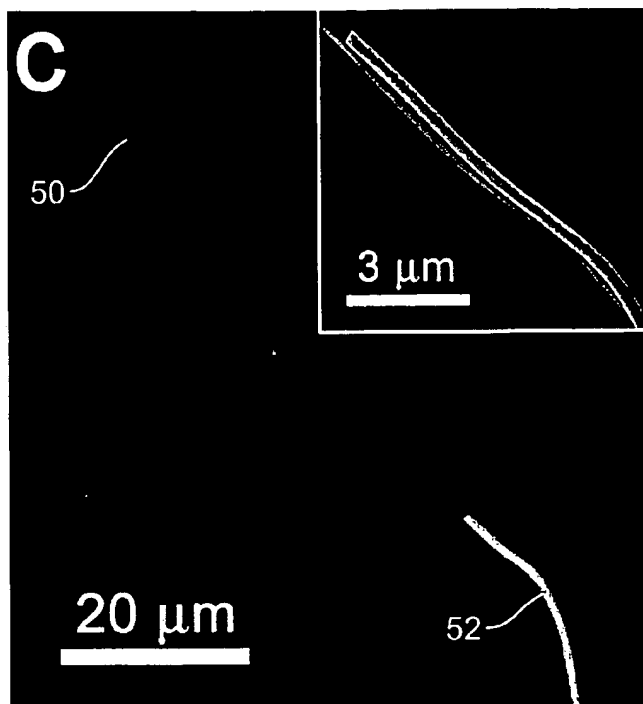


FIG. 17C

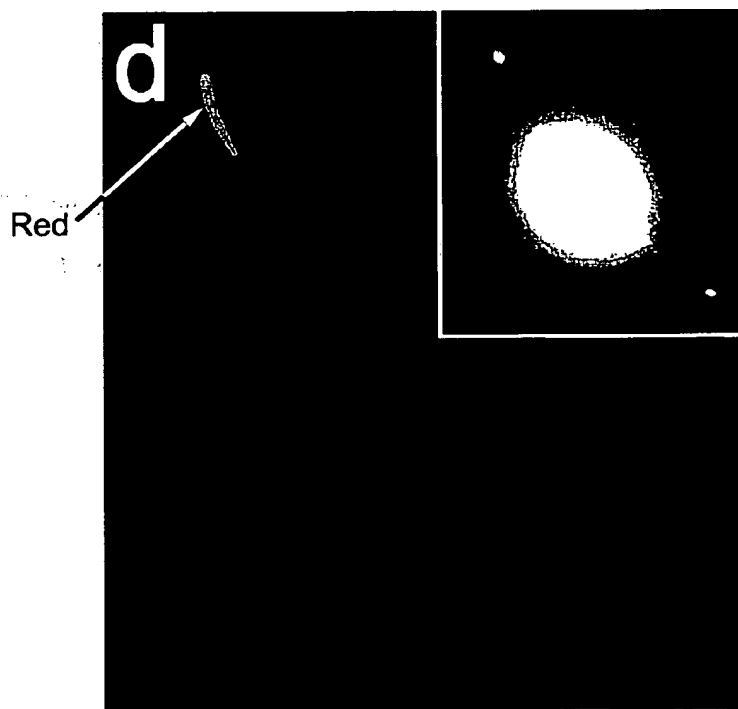


FIG. 17D

27/32

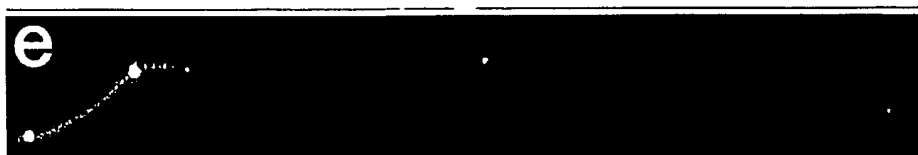


FIG. 17E

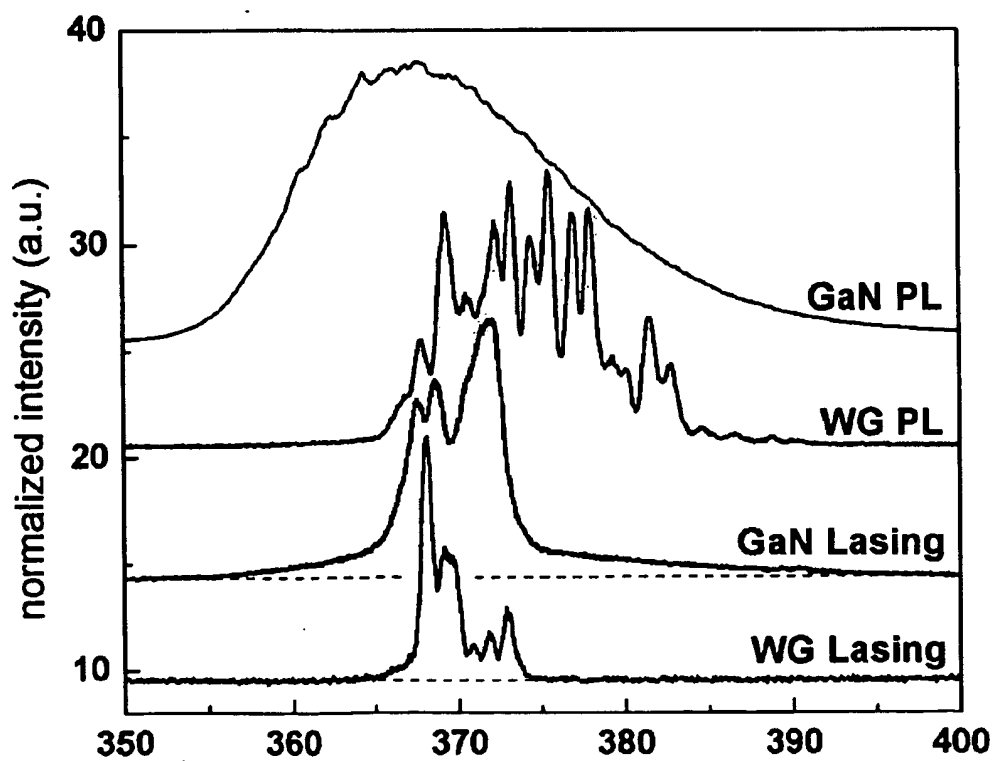


FIG. 17F

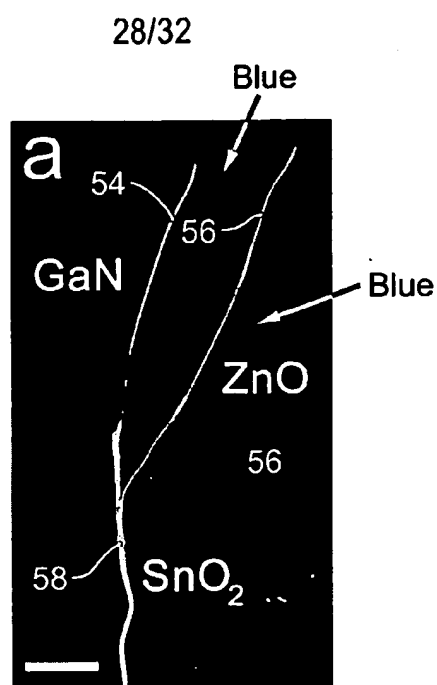


FIG. 18A

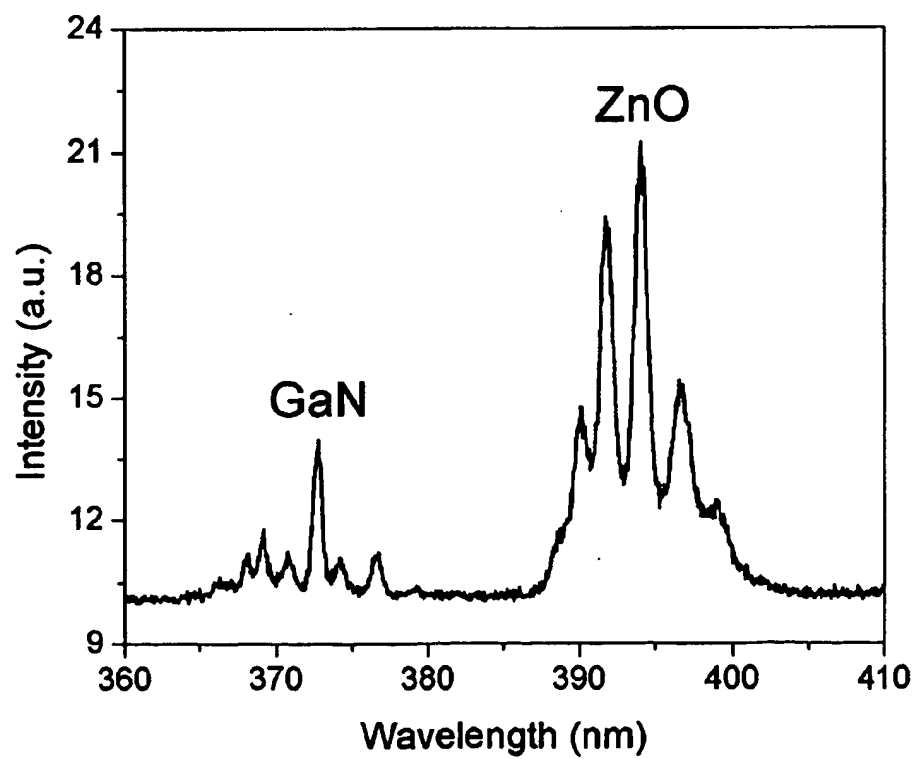


FIG. 18B

29/32

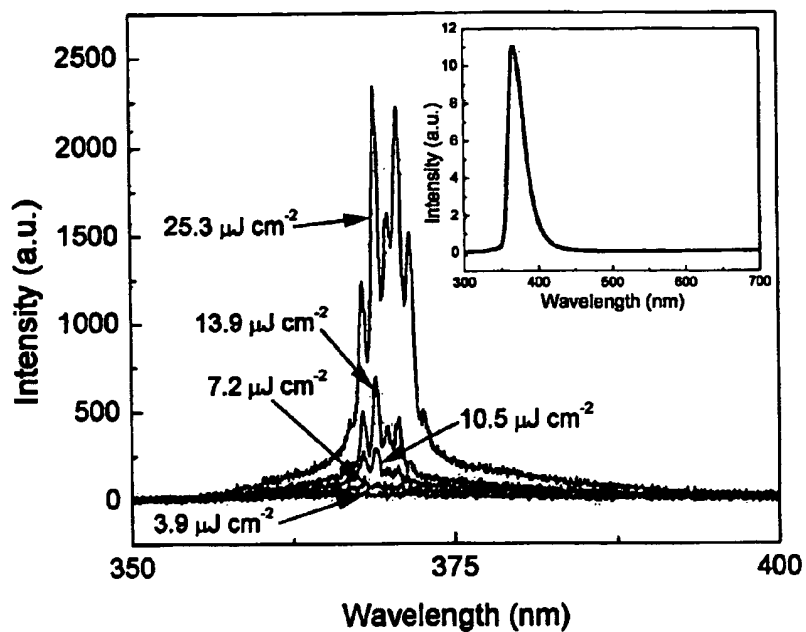


FIG. 19A

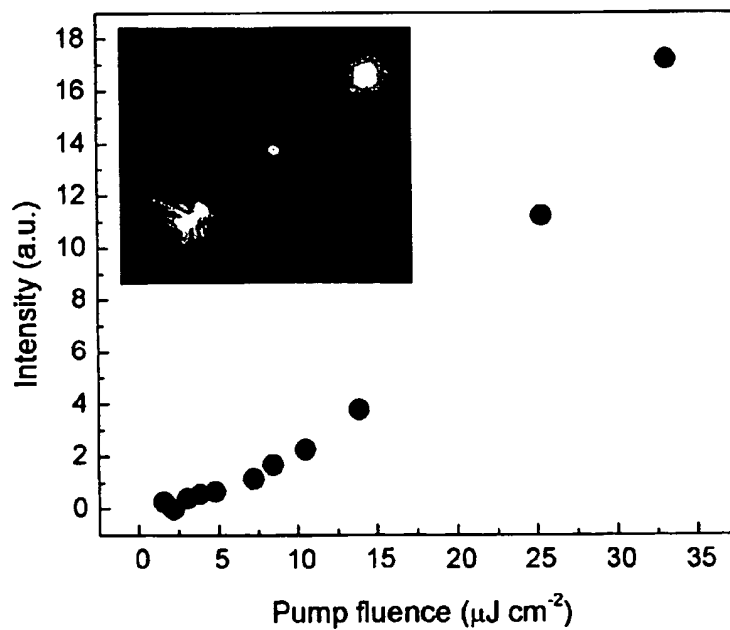


FIG. 19B

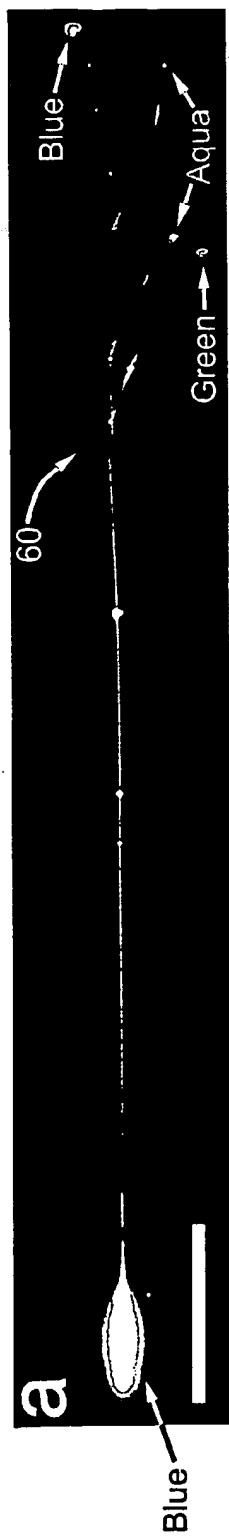


FIG. 20A

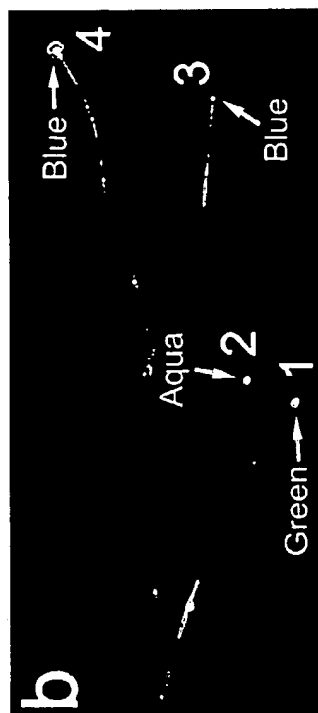


FIG. 20B

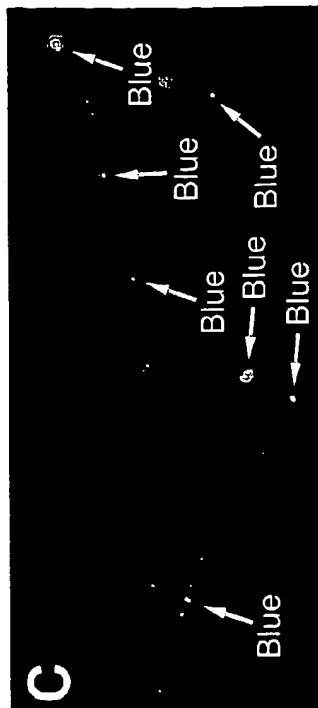


FIG. 20C

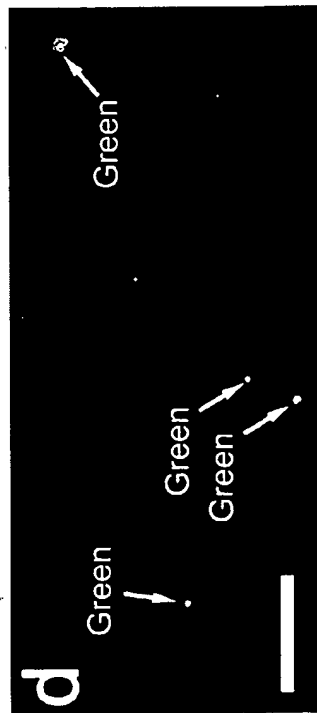


FIG. 20D

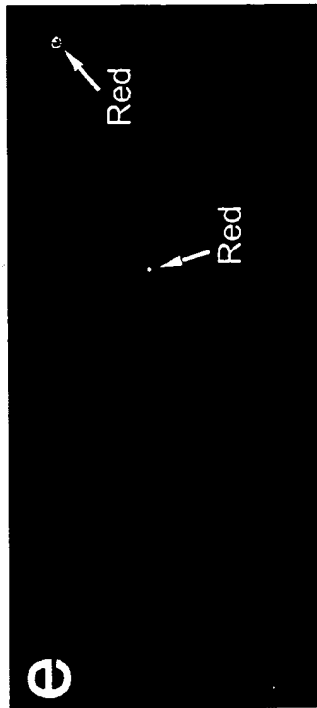


FIG. 20E

31/32

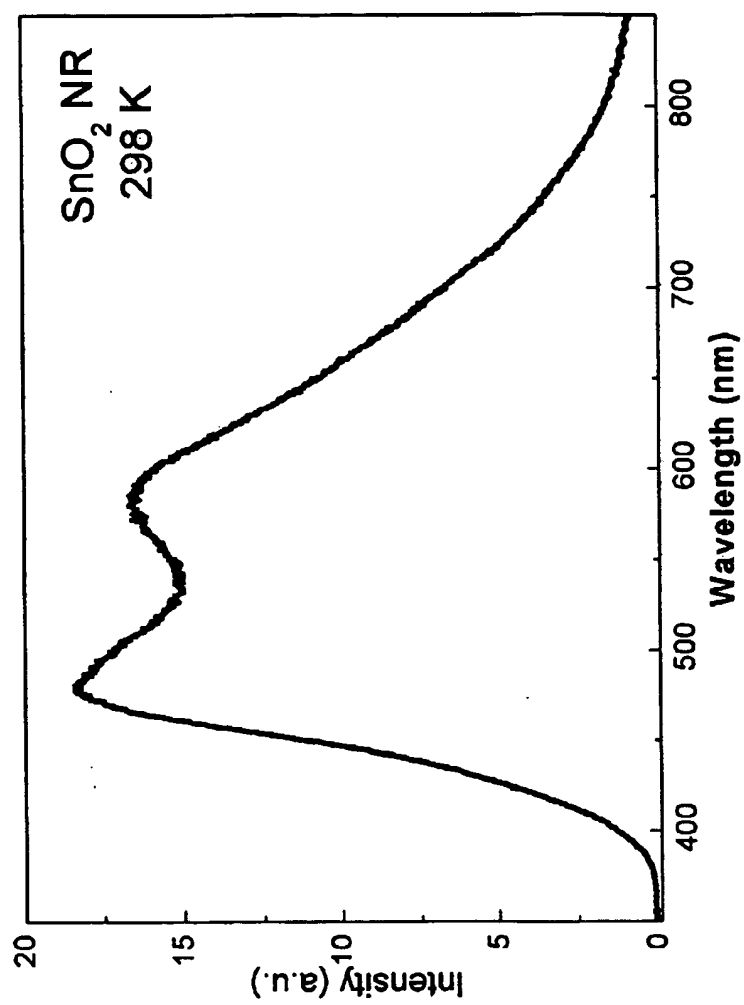


FIG. 21

32/32

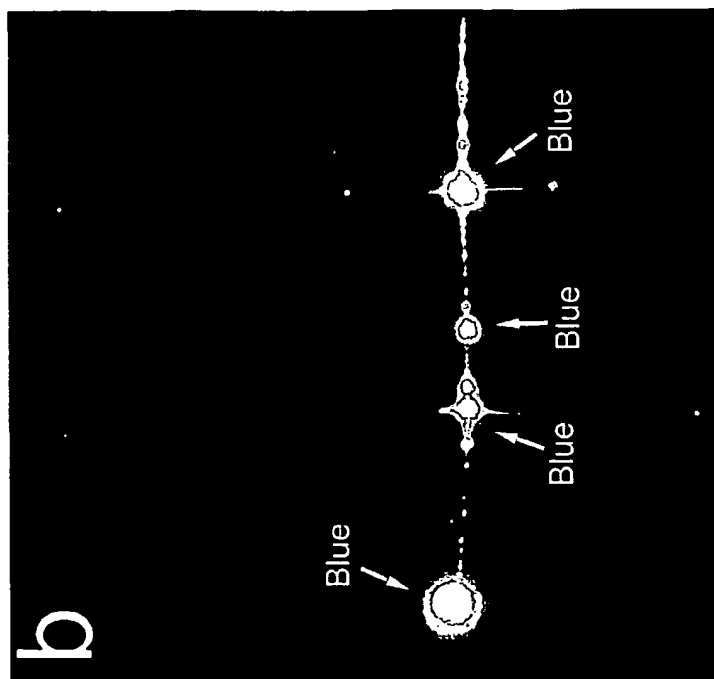


FIG. 22B

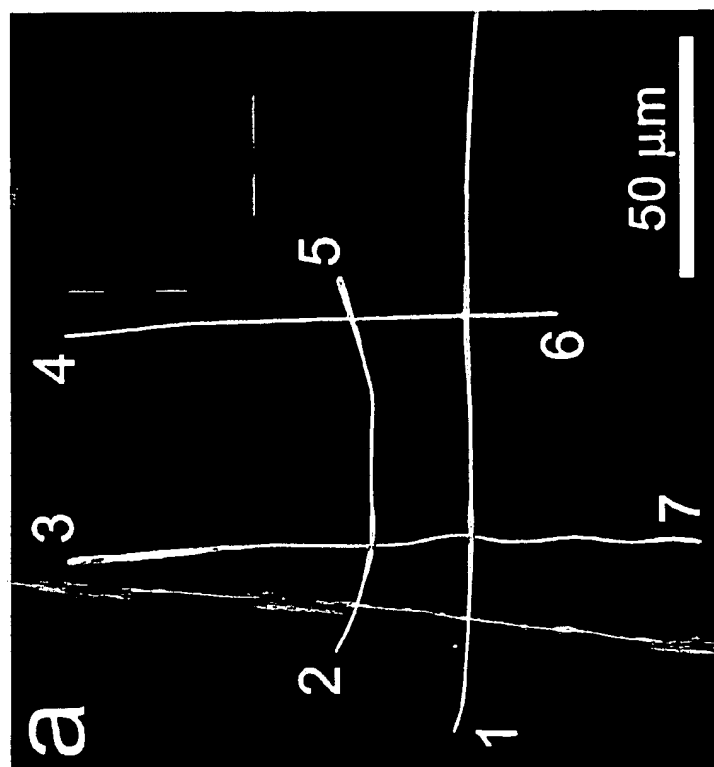


FIG. 22A

This Page Blank (uspic)

Lasing in Single Cadmium Sulfide Nanowire Optical Cavities

Ritesh Agarwal,[†] Carl J. Barrelet,[†] and Charles M. Lieber^{*,†,‡}

Department of Chemistry and Chemical Biology and Division of Engineering and Applied Sciences, Harvard University, Cambridge, Massachusetts 02138

Received March 7, 2005

ABSTRACT

The mechanism of lasing in single cadmium sulfide (CdS) nanowire cavities was elucidated by temperature-dependent and time-resolved photoluminescence (PL) measurements. Temperature-dependent PL studies reveal rich spectral features and show that an exciton–exciton interaction is critical to lasing up to 75 K, while an exciton–phonon process dominates at higher temperatures. These measurements together with temperature and intensity dependent lifetime and threshold studies show that lasing is due to formation of excitons and, moreover, have implications for the design of efficient, low threshold nanowire lasers.

Semiconductor nanowires (NWs) are emerging as versatile nanoscale building blocks for the assembly of photonic devices,^{1–4} including polarization sensitive photodetectors,² light emitting diodes,³ and electrical injection lasers.⁴ Progress on such nanophotonic devices will require developing a detailed understanding of how confinement of charge carriers and photons affects optical properties and/or gives rise to interesting phenomena.^{4–6} For example, single NWs have recently been shown to function as optical waveguides and Fabry–Perot cavities.^{4,7} Intense optical excitation of single NWs has produced stimulated emission and lasing,^{4,8,9} and, significantly, lasing has also been obtained from cadmium sulfide (CdS) NW electrical injection devices.⁴ The mechanism of lasing in these confined NW cavities is unclear, although critical to the rational development, for example, of ultralow threshold NW lasers.

CdS nanowires are particularly interesting since optical excitation and electrical injection have been used to exceed the threshold for lasing.⁴ In bulk CdS, three different mechanisms are known to produce significant gain: exciton–exciton scattering; exciton–longitudinal optic (ex-LO) phonon scattering; and exciton–electron scattering.^{10–13} The geometry and quality¹⁴ of the bulk CdS materials have been found to affect the mechanism yielding the highest gain and lasing, and, importantly, it is expected that geometrically confining cavities might also significantly affect the gain mechanism and lasing.^{6,15} In this letter we report detailed temperature-dependent and time-resolved PL measurements that define the mechanism of lasing in single nanowires for the first time. PL studies of CdS NW optical cavities, which have

diameters smaller than the wavelength of light but large enough to sustain a single optical mode, demonstrate that exciton–exciton scattering is critical to lasing up to 75 K and that an exciton–phonon process dominates at higher temperatures. These measurements together with intensity dependent PL, lifetime, and threshold studies imply that lasing is due to the formation of excitons and not an electron–hole plasma at all of the temperatures and intensities studied.

Single-crystal CdS NWs with diameters from 80 to 150 nm and lengths up to 100 μm were prepared by a metal nanocluster catalyzed vapor–liquid–solid growth,¹⁶ and subsequently dispersed on Si/SiO₂ substrates (600 nm thermal oxide) with an average separation of 100 μm . PL experiments were carried out by exciting the NWs using frequency doubled Ti:sapphire laser pulses (~ 405 nm, 350 fs fwhm) focused to a diameter of ~ 75 μm . PL spectra from individual NWs were recorded from the ends of the NW cavity as illustrated schematically in Figure 1a using a home-built epifluorescence microscope (60 \times , 0.7 NA objective) with a spectral resolution ca. 0.15 nm. A typical PL image of a NW excited by a tightly focused laser (Figure 1b) exhibits emission from the excitation region and 20 μm away at the NW end, thereby demonstrating excellent waveguiding of the CdS NWs. Below we focus on the emission from the NW ends.

PL spectra recorded at 4.2 K from a 40 μm long, ca. 100 nm diameter CdS NW as a function of excitation power are shown in Figure 1c; similar results were observed for NWs with 80–150 nm diameters and 30–50 μm lengths. The PL spectrum recorded at low excitation intensity of 0.6 nJ/cm² (Figure 1c) reveals a number of well-defined and reproducible features in the 488 to 530 nm range, with peaks at 488.8,

* Corresponding author. Email: cml@cmliris.harvard.edu.

[†] Department of Chemistry and Chemical Biology.

[‡] Division of Engineering and Applied Sciences.

This Page Blank (uspto)

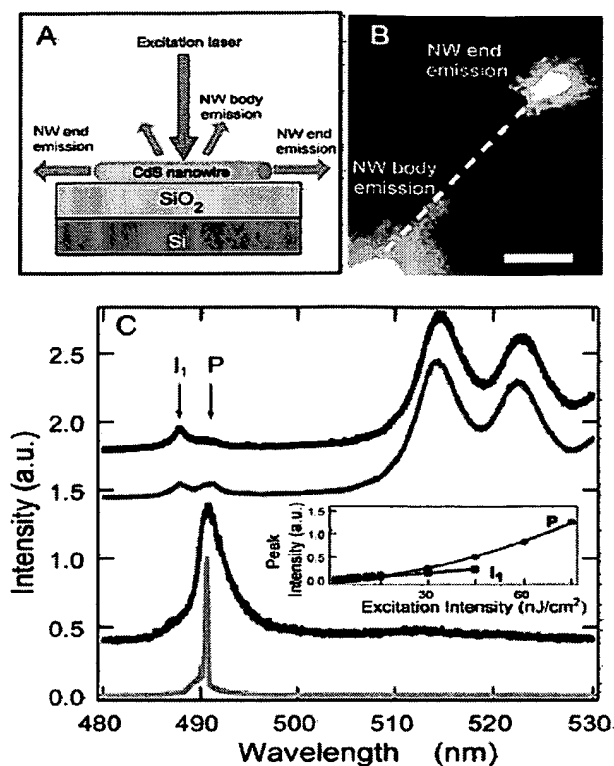


Figure 1. (A) Schematic of single NW optical experiments. (B) PL image showing luminescence from the excitation area (lower left) and one end (upper right) of a CdS NW. The NW was excited with a focused beam ($\sim 5 \mu\text{m}$ diameter) with a power of 10 nJ/cm^2 ; scale bar, $5 \mu\text{m}$. (C) PL spectra of CdS NW end emission recorded at 4.2 K with excitation powers of 0.6 , 1.5 , 30 , and 240 nJ/cm^2 for the black, blue, red, and green curves, respectively. Inset shows peak intensity of I_1 (black squares) and P (red circles) bands vs incident laser power. Solid lines are fits to experimental data with power exponents of 0.95 for I_1 and 1.8 for P .

490.5 , 513 , 522 , and 530 nm . Comparison to previous studies of bulk CdS crystals suggests that the peaks at 488.8 (I_1), 490.5 nm (P), 513 , and $522/530 \text{ nm}$ correspond to neutral acceptor bound excitons,¹⁷ exciton-exciton scattering,¹⁸ free electron-bound hole radiative recombination, and the LO phonon progressions of the free electron-bound hole transitions,¹⁹ respectively.

Excitation power dependent measurements (Figure 1c) show that the P-band intensity increases rapidly and becomes dominant at higher excitation powers. Analysis of the P-band data shows an intensity increase of ~ 1.8 , where I is the excitation intensity (inset, Figure 1c), while the I_1 band increases with an exponent near unity (0.95). These exponents are close to the values expected for 2- and 1-exciton processes.^{10,18} At higher excitation intensities the P-band is the dominant feature in PL spectra (Figure 1c) and furthermore shows a superlinear increase in the PL intensity above a threshold pumping power of 200 nJ/cm^2 . Above this threshold the PL spectrum collapses to a narrow peak at 490.5 nm with a line width of 0.3 nm , indicative of lasing. The position and the power dependence of the PL spectrum strongly suggest that the mechanism of lasing in CdS NWs at 4.2 K is due to an exciton-exciton process. Although

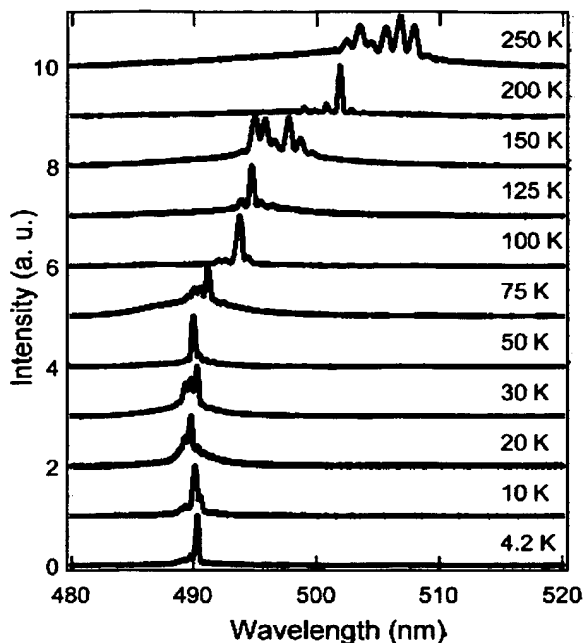


Figure 2. Temperature-dependent spectra recorded from a single CdS NW above the threshold for lasing. The temperature values are given next to each spectrum. The excitation power ranges from $0.24 \mu\text{J/cm}^2$ at 4.2 K to $3.3 \mu\text{J/cm}^2$ at 250 K .

previous studies reported line narrowing at 490 nm ,⁴ these studies did not identify the origin of the lasing peak.

Temperature dependent spectra, which were recorded to probe further the mechanism of lasing in the CdS NWs, show that the lasing line at 490.5 nm is temperature independent from 4.2 to 75 K , while the spectral features associated with lasing exhibit a pronounced red-shift at high temperatures (Figure 2). A summary of these temperature dependent results (Figure 3a) shows clearly the temperature independence of the 490.5 nm peak above threshold at low temperatures, and the subsequent monotonic red-shift at 0.083 nm/K above ca. 100 K . Below the threshold for lasing the main PL peak at 490.5 nm was also found to be temperature independent up to ca. 100 K . Above 100 K the PL peak shifts to ca. 494 nm and then further red-shifts at a rate similar to that observed above threshold. The peak at 494 nm has been assigned previously to an exciton-LO band.¹¹⁻¹⁴ The laser threshold temperature dependence (Figure 3b) shows that the threshold power increases very slowly until 50 K ($4.5 \text{ nJ/cm}^2/\text{K}$) and then increases at a $\sim 3\times$ higher rate of $14 \text{ nJ/cm}^2/\text{K}$.

The observation of the dominant lasing line at 490.5 nm up to 75 K shows that exciton-exciton scattering is the key gain mechanism for CdS NW optical cavities in this lower temperature regime. This temperature independence is consistent with the ca. 20 meV separation between the $n = 1$ ground state and $n = 2$ state.¹² Hence, $n = 2$ and higher exciton states are not significantly populated over this temperature range, and the dominant lasing line should not vary strongly with temperature as we observe. In addition, measurements of the threshold power dependence for our CdS NW system (Figure 3b) show little temperature depen-

This Page Blank (uspto)

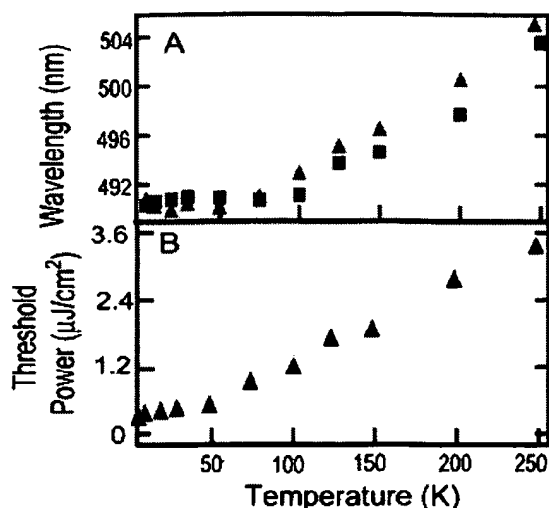


Figure 3. (A) Temperature dependence of key spectral features above and below the threshold for lasing. Red triangles correspond to the temperature dependence of the most prominent lasing peak (for multiple peaks of comparable intensity the central peak). Black squares correspond to temperature dependence of the PL peaks that lead to lasing. These latter data were recorded at low excitation powers, ranging from 25 nJ/cm^2 (4.2 K) to 125 nJ/cm^2 (250 K). (B) Temperature dependence of laser threshold power.

dence below 75 K, which is also consistent with our assignment of lasing from $n = 1$ excitons.

At temperatures above 75 K, higher exciton states become thermally populated and lead to increases in the lasing threshold for the exciton–exciton process. Exciton–scattering by LO phonons can contribute more to gain at these temperatures since the LO phonon energy, 38 meV, is larger than the available thermal energy.^{11–13} Significantly, at temperatures >75 K the PL band and laser lines occur in the region of the ex-LO phonon scattering band, 493 nm.^{12,13} Temperature-dependent measurements (Figure 3a) further show a red-shift, 0.083 nm/K, consistent with that observed in bulk CdS,¹³ 0.086 nm/K, for the ex-LO phonon band. Therefore, at temperatures higher than 75 K the lasing mechanism of CdS NWs can be assigned to ex-LO phonon scattering process.

In contrast, lasing in bulk CdS crystals has been primarily attributed at higher temperature to an exciton–electron scattering process.^{10–13} The exciton–electron scattering band appears at ~ 494 nm at 70 K and exhibits a large red-shift of ca. 0.147 nm/K.^{12,13} The temperature-dependent red-shift we find for CdS NWs, 0.083 nm/K, is much smaller than this but agrees with the ex-LO process (see above). We believe that the difference between previous bulk studies and these new NW lasers arises from the small modal volume of the laser cavity.²⁰ To understand this unique difference a simple model based on the density of states of electrons and excitons at equilibrium was used to calculate the ratio of free carriers to the total injected carriers in the cavity as a function of temperature (Figure S1, Supporting Information). These results show that at 150 K temperatures and low carrier densities (10^{15} – 10^{16} cm^{-3}) $> 80\%$ of the carriers exist as free electrons, whereas at higher densities (10^{18} cm^{-3}) the

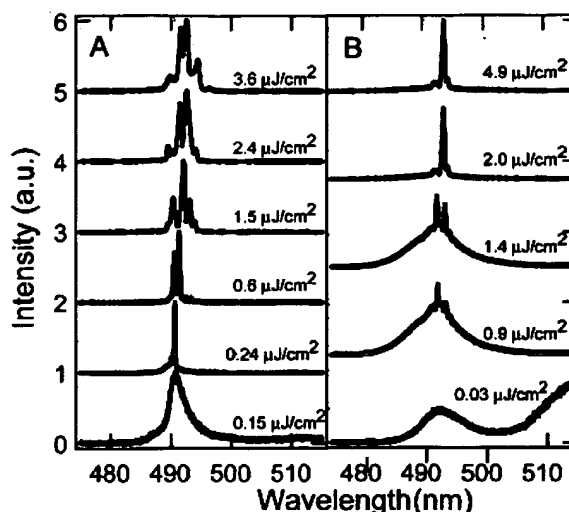


Figure 4. Spectra recorded above the lasing threshold for a CdS NW at different pumping powers at 4.2 K (A) and 100 K (B). The bottom spectrum in both the panels is the PL recorded below the threshold for lasing.

free carriers do not exceed 40%. The small volume of the NW laser cavity can effectively yield large carrier densities, and hence the portion of free carriers is smaller than in bulk samples, thus reducing contributions from exciton–electron scattering.

In addition, we find that the laser threshold power for CdS NWs is 5–10 times less sensitive to temperature than reported for bulk CdS crystals.^{21,22} The linear increase of the lasing threshold power with temperature due to ex-LO mechanism of lasing cannot be explained by a simple model based on the temperature dependence of the occupation of the phonon states as this model predicts an exponential increase in the threshold. We believe this disagreement can be attributed to the strong confinement of the optical mode in the CdS NW cavity, where there is $\sim 50\%$ mode confinement due to strong dielectric mismatch between the wire and its surroundings.²³ Strong mode confinement in optical cavities leads to much better overlap of the optical mode with excitons, where the modal volume of the NW cavity is of the order of $(3\lambda)^3$.²⁰ This observation is similar to the reduced magnitude and lower temperature dependence of the laser threshold observed in double heterostructure planar semiconductor lasers,²⁴ although the mode confinement is typically only a few percent. Future theoretical analysis, which includes the effect of strong optical confinement¹⁵ along with the exciton–LO scattering mechanism for gain, will be required to explain the weak temperature dependence of lasing threshold observed for CdS NWs.

We have also investigated the possibility of lasing from an electron–hole plasma, which can form due to screening of excitons at high carrier densities ($n \sim 2.1 \times 10^{18}$ cm^{-3})²⁵ by recording spectra as a function of different pumping powers above the threshold for lasing. Significantly, no red-shift of the lasing line was observed at either 4.2 or 100 K while increasing the excitation intensity approximately an order of magnitude (Figure 4). An estimate of the carrier

This Page Blank (uspto)

density based on laser pump intensity ($5 \mu\text{J}/\text{cm}^2$), CdS NW dimensions ($40 \mu\text{m}$ length, 100 nm diameter), CdS absorbance at 400 nm ($\sim 10^5 \text{ cm}^{-1}$) gives a value of $n \sim 1.0 \times 10^{18} \text{ cm}^{-3}$, which is close to the threshold reported²⁵ to yield dissociation into an electron–hole plasma.

Formation of electron–hole plasma is generally accompanied by a strong red-shift of the spectrum due to band-gap renormalization effect^{13,26} and has been suggested for GaN nanowires.⁷ The absence of a red-shift with increasing excitation intensity is a further proof of lasing by excitonic mechanism in the range of the excitation intensities used in our study. In addition, excited state PL lifetime measurements (data not shown) did not show significant pump intensity dependence. The lifetime at 4.2 K was observed to be 1.2 ns (90% amplitude); which rapidly dropped to 400 ps at 50 K and then decayed very slowly to $\sim 350 \text{ ps}$ at room temperature. However, neither the amplitude nor the time scale of the PL lifetime changed more than 10% with $10\times$ (4.2 K) or $5\times$ (100 K) increase in pump intensity. In contrast, previous studies of highly excited bulk CdS samples showed a rapid 200 ps (5 K) lifetime that was attributed to the decay of an electron–hole plasma into excitons.²⁷ The absence of a fast component in our experiments, even at very high pump powers, further rules out the formation of an electron–hole plasma in the CdS NW lasers.

In summary, the mechanism of lasing in single CdS NWs was elucidated by temperature-dependent spectroscopic studies. Our data show that the mechanism is exciton-based: exciton–exciton scattering from 4.2 to 75 K and exciton–LO scattering at higher temperatures. Similar detailed optical studies would be useful for other NW optical cavities, such as ZnO ⁵ and GaN ,⁷ to enable determination of the lasing mechanism, since the mechanism will depend on factors including the crystal properties, cavity configuration, losses, and excited-state lifetimes. We believe our results will help in modeling⁶ the lasing behavior in these novel nanostructures, and also aid in the design of ultralow threshold NW lasing devices. For example, the excitonic mechanism of lasing could be enhanced through of NW laser cavities based on radial NW heterostructures.¹ Specifically, small diameter NWs coated by a larger band-gap material might be used as efficient nanoscale lasing structures, where the small diameter NW provides a low threshold active medium due to exciton confinement, and the outer shell would facilitate waveguiding within a small modal volume optical cavity.

Acknowledgment. C.M.L. acknowledges support of this work by the Air Force Office of Scientific Research and Defense Advanced Research Projects Agency.

Supporting Information Available: Calculated fraction of free carriers/total carriers in a bulk CdS crystal for different carrier densities as a function of temperature. This material is available free of charge via the Internet at <http://pubs.acs.org>.

References

- (1) Lieber, C. M. *MRS Bull.* **2003**, *28*, 486.
- (2) Wang, J. F.; Gudiksen, M. S.; Duan, X. F.; Cui, Y.; Lieber, C. M. *Science* **2001**, *293*, 1455.
- (3) Duan, X. F.; Huang, Y.; Cui, Y.; Wang, J. F.; Lieber, C. M. *Nature* **2001**, *409*, 66.
- (4) Duan, X. F.; Huang, Y.; Agarwal, R.; Lieber, C. M. *Nature* **2003**, *421*, 241.
- (5) Johnson, J. C.; Yan, H. Q.; Yang, P. D.; Saykally, R. J. *J. Phys. Chem. B* **2003**, *107*, 8816.
- (6) Maslov, A. V.; Ning, C. Z. *Appl. Phys. Lett.* **2003**, *83*, 1237.
- (7) Johnson, J. C.; Choi, H.-J.; Knutsen, K. P.; Schaller, R. D.; Yang, P.; Saykally, R. J. *Nat. Mater.* **2002**, *1*, 106.
- (8) Huang, M. H.; Mao, S.; Feick, H.; Yan, H.; Wu, Y.; Kind, H.; Weber, E.; Russo, R.; Yang, P. *Science* **2001**, *292*, 1897.
- (9) Zapien, J. A.; Jiang, Y.; Meng, X. M.; Chen, W.; Au, F. C. K.; Lifshitz, Y.; Lee, S. T. *Appl. Phys. Lett.* **2004**, *84*, 1189.
- (10) A La Guillaume, C. B.; Debever, J.-M.; Salvan, F. *Phys. Rev.* **1969**, *177*, 567.
- (11) Haug, H.; Koch, S. *Phys. Status Solidi B* **1977**, *82*, 531.
- (12) Koch, S. W.; Haug, H.; Schmieder, G.; Bohnert, W.; Klingshirn, C. *Phys. Status Solidi B* **1978**, *89*, 431.
- (13) Fischer, T.; Bille, J. J. *Appl. Phys.* **1974**, *45*, 3937.
- (14) Song, J. J.; Wang, W. C. *J. Appl. Phys.* **1984**, *55*, 660.
- (15) Maslov, A. V.; Ning, C. Z. *IEEE J. Quantum Electron.* **2004**, *40*, 1389.
- (16) Barrelet, C. J.; Wu, Y.; Bell, D. C.; Lieber, C. M. *J. Am. Chem. Soc.* **2003**, *125*, 11498.
- (17) Thomas, D. G.; Hopfield, J. J. *Phys. Rev.* **1962**, *128*, 2135.
- (18) Magde, D.; Mahr, H. *Phys. Rev. Lett.* **1970**, *24*, 890.
- (19) Colbow, K. *Phys. Rev.* **1966**, *141*, 742.
- (20) For CdS NW, $d = 100 \text{ nm}$; $L = 40 \mu\text{m}$, $\lambda = 500 \text{ nm}$; therefore, the volume occupied by the CdS material assuming a cylindrical geometry is $\sim 3\lambda^3$.
- (21) Hvam, J. M. *Phys. Rev. B* **1971**, *4*, 4459.
- (22) Leheney, R. F.; Shaklee, K. L.; Ippen, E. P.; Nahory, R. E.; Shay, J. L. *Appl. Phys. Lett.* **1970**, *17*, 494.
- (23) Mode confinement in a cylindrical waveguide is given by $\eta = 1 - (2.405 \exp^{-1/V})^2/V^{-3}$; $V = k^2(n^2 - 1)/\lambda^2$ and $k = 2\pi/\lambda$. For CdS, $n \sim 2.6$; $\lambda = 500 \text{ nm}$.
- (24) Panish, M. B.; Hayashi, I.; Sumski, S. *Appl. Phys. Lett.* **1970**, *16*, 326.
- (25) Ehrenreich, H.; Seitz, F.; Turnbull, D. *Solid State Physics*; Academic Press: New York, 1977.
- (26) Koch S. W. *Quantum Theory of the Optical and Electronic Properties of Semiconductors*; World Scientific: Singapore, 1993.
- (27) Saito, H.; Gobel, E. O. *Phys. Rev. B* **1985**, *31*, 2360.

NL050440U

This Page Blank (uspto)

**This Page is Inserted by IFW Indexing and Scanning
Operations and is not part of the Official Record**

BEST AVAILABLE IMAGES

Defective images within this document are accurate representations of the original documents submitted by the applicant.

Defects in the images include but are not limited to the items checked:

- ☐ BLACK BORDERS
- ☐ IMAGE CUT OFF AT TOP, BOTTOM OR SIDES
- ☒ FADED TEXT OR DRAWING
- ☐ BLURRED OR ILLEGIBLE TEXT OR DRAWING
- ☐ SKEWED/SLANTED IMAGES
- ☐ COLOR OR BLACK AND WHITE PHOTOGRAPHS
- ☐ GRAY SCALE DOCUMENTS
- ☐ LINES OR MARKS ON ORIGINAL DOCUMENT
- ☐ REFERENCE(S) OR EXHIBIT(S) SUBMITTED ARE POOR QUALITY
- ☐ OTHER: _____

IMAGES ARE BEST AVAILABLE COPY.

As rescanning these documents will not correct the image problems checked, please do not report these problems to the IFW Image Problem Mailbox.

This Page Blank (uspto)